Lund University - Faculty of Engineering

Master Thesis

Solid State Physics

The Effect of Electrode Composition on the Composition of Binary Ag/Au Nanoparticles Produced by Spark Ablation

Linnéa Jönsson

Supervisor:
Maria Messing

Co-Supervisor:
Markus Snellman

Examiner:
Carina Fasth

June 10, 2021

LUND UNIVERSITY

NANO LUND

AT THE FOREFRONT OF NANOSCIENCE

Abstract

Synthesis of nanoparticles with high control of the particle composition, high purity and high throughput is of great interest for multiple applications such as catalysis, medicine, energy storage, sensoring, and electronics. As an alternative method to the traditionally used chemical synthesis routes, gas-phase methods have gained attention due to the avoidance of solvents resulting in higher purity of the particles, but also due to the more flexible choice of materials. Spark ablation is a synthesis process that through ablation of two non-insulating electrodes produces high purity nanoparticles in the gas phase with a high control of the composition. Literature indicates that nanoparticles generated with alloyed electrodes obtain the same composition as the electrodes, but this has not been sufficiently proved. It is, furthermore, stated that nanoparticles produced with two different electrodes have a larger compositional spread than nanoparticles produced with alloyed electrodes.

The composition of spark ablated Ag-Au bimetallic nanoparticles produced in 2017 and 2021 using both alloyed (Ag25Au75, Ag50Au50 and Ag75Au25) and two different electrodes (Ag and Au) has been investigated and compared to the electrode composition. The analysis has included both ensemble (SEM-EDS and XRD) and single particle (TEM-EDS and STEM-EDS) characterization methods, the latter essential for comparing the compositional variance of the nanoparticles but often neglected in the literature.

Here, by using single particle analysis in a sensible way in combination with statistical analysis of the results, we have confirmed that particles produced using alloyed electrodes obtain the same composition as the electrodes. We hope that this accomplishment will inspire the field of spark ablation. General strategies for presenting reliable quantitative analysis of individual particles could simplify interpretation and comparison of results with each other, which could assist the development of high performance nanoparticles attractive for industrial applications.

Acknowledgements

For this master thesis, I have a lot of people to thank. First of all, I want to thank the engineered nanoparticle group at NanoLund for introducing me to the community and for lots of enjoyable weekly meetings on Zoom (or Teams?). Specifically I want to thank Markus Snellman, my second supervisor, for teaching me the aerosol generation system and all its peculiarities.

I also want to thank Martin Ek and Maria Messing for taking beautiful images of my particles in the TEM, and for performing (lots of!) EDS measurements of my particles, when I could not.

Johan Gustafson helped me obtain XRD measurements, even though the light was off in the lab, and I could not have done it without him.

Crispin Hetherington has opened the door at the chemistry centre for me many times, and without him, I would neither have obtained any AZtec data, nor been able to enter the building. He has also taken the time to answer my questions about microscopes and compositional analysis, and for that I am very thankful.

I could not have wished for a more excellent first supervisor, or one that is faster at giving feedback. Thank you Maria, for making this semester a both educative and exciting experience!

Lastly, I want to thank my friends, family, and Jonas.

My friends, for the Friday lunches, ventilation, and Pore Solutions.

My family, for being the best family one could ever wish for.

My Jonas, for all the support, love, and knowledge about statistics.

List of Abbreviations

DMA Differential Mobility Analyzer

EDS Energy Dispersive X-ray Spectroscopy

ESP Electrostatic Precipitator

ICP-MS Inductively Coupled Plasma-Mass Spectrometry

ICP Inductively Coupled Plasma

SDG Spark Discharge Generator

SEM-EDS Scanning Electron Microscopy-Energy Dispersive X-ray Spectroscopy

SEM Scanning Electron Microscopy

STEM-EDS Scanning Transmission Electron Microscopy-Energy Dispersive X-ray Spectroscopy

STEM Scanning Transmission Electron Microscopy

TEM-EDS Transmission Electron Microscopy-Energy Dispersive X-ray Spectroscopy

TEM Transmission Electron Microscopy

XPS X-ray Photoelectron Spectroscopy

XRD X-Ray Diffraction

Populärvetenskaplig sammanfattning

Vad finns överallt omkring oss, är osynligt för blotta ögat och har stor potential att förändra världen? Kanske kommer du att tänka på olika sorters magi, men ett något mer konkret svar på gåtan är *nanopartiklar*. Dessa små materialbitar, i storleksordningen 1 – 100 miljarddels meter, har visat sig ha egenskaper som skiljer sig från större partiklar av samma material och tros kunna bidra till applikationer inom bland annat elektronik, batterier, sensorer, katalysatorer och medicin. En metod som kan producera nanopartiklar är *gnistablation*. Fördelar med just denna metod jämfört med en av de vanligaste metoderna, kemisk syntes, är bland annat att partiklarna är fria från produktionsrester men också att man kan blanda material med varandra som normalt sett inte är möjligt. Det är exempelvis inte möjligt att blanda silver och koppar i vilken kombination som helst, men på nanoskalan, med hjälp av gnistablation, är det möjligt!

För att kunna utnyttja nanopartiklar, och speciellt nanopartiklar bestående av två eller flera material, krävs hög kontroll över dess storlek och form, men framförallt dess komposition, hur mycket av varje material som varje enskild nanopartikel innehåller. Dessa faktorer spelar stor roll för partiklarnas egenskaper, och kan man styra dem, kan man också styra egenskaperna! Ett exempel på detta är magnetiska nanopartiklar som består av lantan, järn och kisel. Genom att justera hur mycket av de olika ämnena som nanopartiklarna består av, kan man justera deras magnetiska egenskaper. Ett annat exempel är nanopartiklar av guld och platina. Genom att justera mängden guld får partiklarna olika hög katalytisk förmåga och kan användas för att underlätta olika kemiska reaktioner. I de båda ovan nämnda exempel har man hittat en optimal komposition som ger de bästa magnetiska egenskaperna respektive den mest fördelaktiga katalytiska förmågan. Det är tydligt att det inte bara är viktigt att medelkompositionen hos alla partiklar är rätt komposition, utan också att alla individuella nanopartiklar har rätt komposition för att kunna bidra med rätt egenskaper.

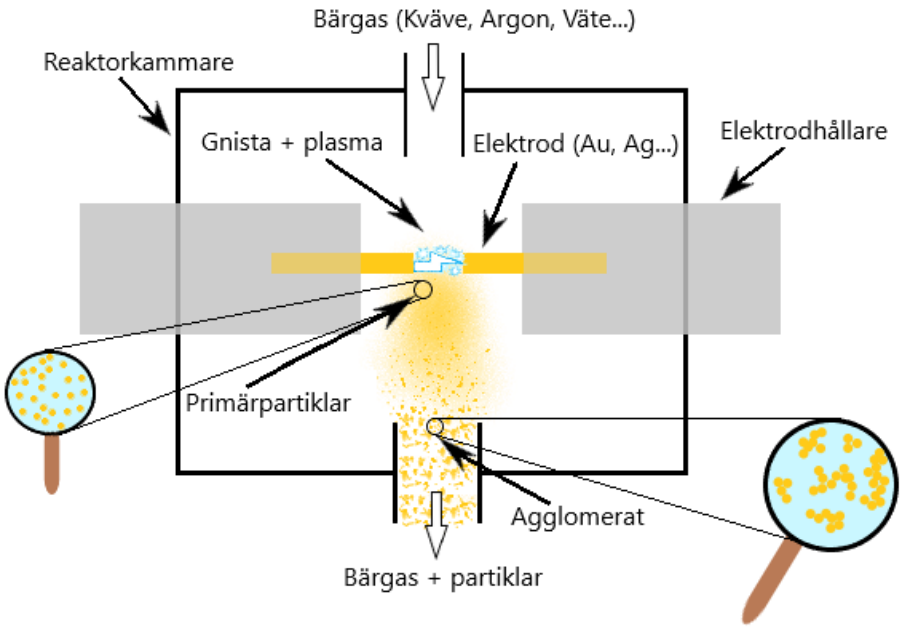

Figure 1: *En skiss av principen för gnistablation.*

När man producerar nanopartiklar med hjälp av gnistablation använder man sig av två ledande elektroder, se figur 1 ovan. Genom att låta en energirik gnista uppstå mellan elektroderna kan man få ut små fragment av de båda elektroderna och dessa fragment kommer därefter att blanda sig med varandra. I mitt fall vill jag ha nanopartiklar som består av två material, guld och silver. Ett sätt att göra det på är att använda elektroder bestående av en guld-silver legering, exempelvis en legering av 50% guld och 50% silver. Ett annat sätt är att använda en elektrod av guld, och en elektrod av silver. När fragmenten från dessa material blandas fås nanopartiklar bestående av en guld-silver blandning.

Hur mycket guld och silver som nanopartiklarna i genomsnitt innehåller då man använder elektroder av olika material tycker man sig kunna beräkna med hjälp av olika produktionsparametrar, och det finns flera studier som pekar på att kompositionen hos nanopartiklarna blir samma som elektroderna då legerade elektroder används. Man har också rapporterat om att kompositionen varierar mer mellan nanopartiklar som producerats med två olika elektroder jämfört med legerade elektroder. Det finns dock inga studier som systematiskt undersökt detta närmare. Något som också bör tilläggas är de mätmetoder som används vid analys av partikelkompositionen. Många gånger analyseras endast medelkompositionen av alla partiklar, detta trots att det inte är känt hur stor varians som finns mellan de individuella partikelkompositionerna. Som vi såg i tidigare avsnitt så är kompositionen av stor vikt hos nanopartiklar då den är starkt relaterad till dess egenskaper. För att undersöka denna varians i komposition närmare har jag undersökt kompositionen av nanopartiklar innehållande guld och silver som producerats med hjälp av gnistablation. Nanopartiklarna framställdes både av olika guld-silver legeringar, och med en guld och en silver elektrod.

Genom att undersöka individuella partikelkompositioner på ett förnuftigt sätt i kombination med enkel statistisk analys av resultaten, har vi bekräftat att partiklar som produceras med legerade elektroder erhåller samma komposition som elektroderna. Vi hoppas att denna prestation, men framförallt detta tillvägagångssättet, kommer att inspirera och hjälpa utvecklingen av gnistablerade nanopartiklar med hög prestanda och som är attraktiva för industriella applikationer.

Contents

1 Introduction

As a part of his doctoral thesis in 1905, Einstein measured the size of a sugar molecule and found it to be about 1 nanometer (10^{-9} m) in diameter [1]. Nanomaterials have a dimension of 1 to 100 nanometers and the term *nanoscience* refers to the manipulation of matter on the nano-scale, where properties differ significantly from those at larger scales. One type of nanomaterial which has found applications in catalysis, medicine, energy storage, sensors, and electrics, to mention a few, is nanoparticles. By controlling the particles' size, morphology and composition, one can control their properties [2]. One example is magnetic nanoparticles consisting of lanthanum, iron and silicon; by tuning how much of each material the particles contain, their magnetic properties can be altered and fit to a desired application [3]. A production method that allows for high control of the nanoparticle composition is spark discharge, or spark ablation.

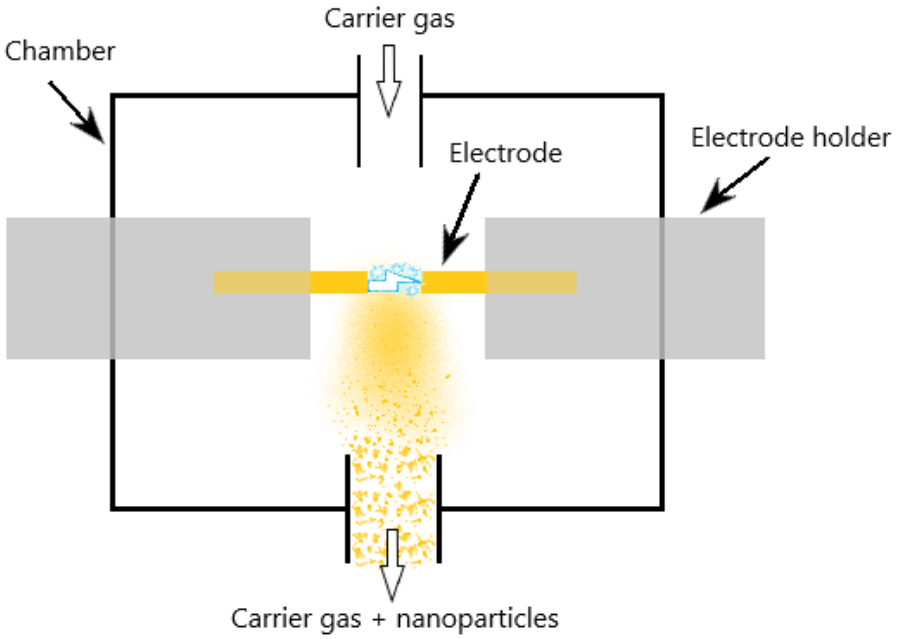

Figure 2: *Schematic of the spark ablation principle.*

Spark ablation is a so-called top-down production method where bulk material is rendered into nano-sized particles. Here, the bulk consists of two opposing electrodes, and by producing a spark between them, electrode material evaporates, mixes and condenses into nanosized particles, see figure 2 above. One of the most important advantages with the method is the ease of producing mixed particles, even with materials that are immiscible in bulk, enabling a myriad of new material combinations on the nanoscale [4][5]. To produce mixed nanoparticles with spark ablation, the most common methods are to use either alloyed electrodes, or electrodes of different materials, e.g., one electrode of gold and one of silver, resulting in nanoparticles of some composition.

As previously mentioned, the nanoparticle composition is of great importance for its properties, and therefore it is of high interest to know how it is decided. One of the main parameters known to affect spark ablated particles' composition is the electrode composition, however, despite efforts, the relation is still not clear. In an attempt to bridge the knowledge gap, the aim of this thesis is to investigate how the composition of alloyed electrodes of gold and silver (Ag25Au75, Ag50Au50

and Ag75Au25) affects the resulting particle composition, and compare it to particle compositions obtained using one electrode of gold and one of silver. The produced particles are analyzed using both average (Scanning Electron Microscopy-Energy Dispersive Spectroscopy (SEM-EDS), X-ray Diffraction (XRD)) and individual particle (Transmission Electron Microscopy-EDS (TEM-EDS), Scanning Transmission Electron Microscopy-EDS (STEM-EDS)) techniques. Data obtained in both 2017 and 2021 will be analyzed and compared to previous results in the literature.

1.1 Nanoparticles

A nanoparticle with a diameter of 10 nm has about 15% of its atoms on the surface and, by comparison, this drops to <1% for a bulk solid [1]. Due to this large surface-to-volume ratio and various associated quantum confinement effects, nanoscale materials behave differently than macroscale (bulk) materials do. One example is gold, which in bulk form is inert, while gold nanoparticles exhibit reactive properties. Another is silver, which in the form of a nanoparticle shows antibacterial properties, and not true for bulk silver [6]. Other behaviour changes on the nanoscale include materials' magnetic, electrical, mechanical, thermodynamic and plasmonic abilities.

Besides changing the size and morphology of a nanoparticle, one can also produce particles made of two or more elements in different compositions to obtain new unique particle behaviors. It has been shown that in many cases, for certain applications, mixed nanoparticles exhibit better characteristics compared to any monometallic ones [2][6]. Numerous bimetallic particles have been developed and are already used in various applications [7]. One example is alloyed Pt–Ru nanoparticles which have been shown to be more resistant to deactivation than pure platinum ones, and can be used as catalysts in fuel cells [6].

Though there are several hundred nanoparticle fabrication methods to choose from [6], they can be categorized as variations of mechanical milling, chemical synthesis, and physical processing [8]. In mechanical milling, bulk material is grinded into nanosized particles using ceramic or metal balls as grinding medium [1]. However, drawbacks to the otherwise simple method include problems with contamination from the grinding material and agglomeration, coalescence, of the particles, due to the long processing time [8]. In chemical processes, metal salts are often reduced in an aqueous or oil solution to produce nanoparticles with high both production rate and size control [8]. However, for every new mixture, a new recipe has to be developed, and post-synthesis steps to get rid of contaminants are practically unavoidable when a liquid phase is used [2]. Physical methods are often more expensive than the above mentioned, but since no chemicals are involved and the particles are suspended in an inert carrier gas, both agglomeration and contamination can be avoided [8]. Common physical methods include flame pyrolysis, laser ablation and spark ablation, the latter being the only technique able to easily produce mixed particles with a diameter below 20 nm [2] and also the method used in this thesis. Furthermore, the investment needed for spark ablation is considerably lower than for laser ablation, and the technique has been shown to be scalable for industrial use [2].

1.2 Spark Ablation

Along with the development of the combustion engine, spark plugs were used, and led to the first studies of ablation, however, as a parasitic effect [9]. The first detailed description of the spark ablation method came first in 1988 [10] and the interest in the technology has since continued to increase, see figure 3 below.

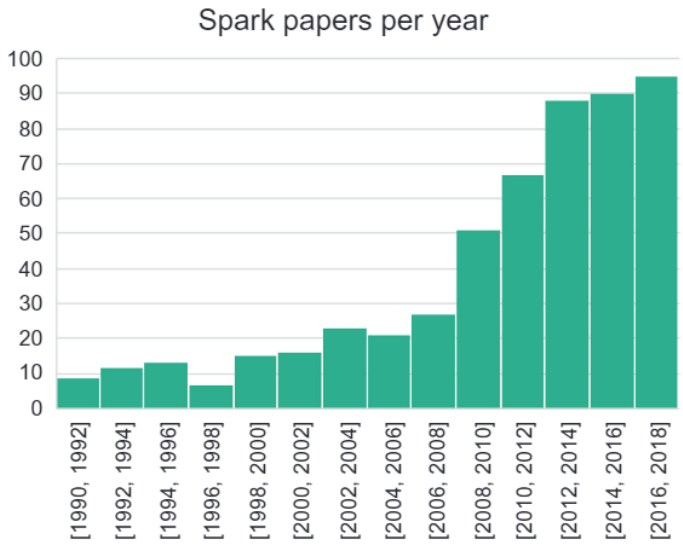

Figure 3: *Number of published spark ablation papers in two year increments from 1990 to 2018. Figure taken from [2].*

The reasons for the growing interest in spark ablation are many. Particles produced in the gas phase are easily manipulated, e.g., oxidized, size-selected or rendered into a core-shell structure. Another advantage is that there is no need to store the particles and since the machine is transportable, they can be produced on site. The technique is also considered environmentally friendly as it does not produce any hazardous waste [11]. Moreover, spark ablation is simple in the sense that it only uses a few production parameters, and flexible in the sense that it can produce nanoparticles of any combination of non-insulating materials that can be shaped into an electrode [2][12][13]. The theory and detailed operating principle of spark ablation, or spark discharge, can be found in chapter 2.

The feasibility of producing mixed or alloyed nanoparticles by spark ablation has led to a high research interest in the technique and in controlling the resulting nanoparticle composition, especially when electrodes of different materials are being used [2][4][13][14][15]. It has for instance been shown that the cathode will be more eroded than the anode due to the nature of the spark, and there are efforts being made in manipulating this phenomena to control the particle composition. Literature indicates that alloyed electrodes generate identical composition in the particles as in the electrodes, and that spark mixing, when two different electrodes are used, leads to a broader variation in the composition of the produced particles. Ways to influence the standard deviation to a smaller value are also proposed [2]. The effect and difference between using alloyed or two different electrodes on the nanoparticle composition has to our knowledge, however, never been investigated systematically, and accompanied with reliable compositional analysis of both individual and average particle compositions.

1.3 Composition of Mixed Particles

To produce mixed nanoparticles with spark ablation, one can choose one of three methods. Either alloyed, two different or so called mixed electrodes made of micrometer sized grains pressed and sintered together, are used. Though there are a few reports available that have investigated the relation between electrode composition and particle composition for some material systems, they are inconsistent, and the relation is still not clear [16]. The inconsistency referred to here is mainly due to inadequate compositional analysis, where individual particle composition is given little consideration compared to more general ensemble measurements [16].

There are several ways to obtain ensemble measurements of nanoparticles' composition, some examples often used in spark ablation literature being SEM-EDS, Inductively Coupled Plasma-Mass Spectrometry (ICP-MS) and XRD. The most frequently used tools for individual particle compositional analysis are TEM-EDS and STEM-EDS, which are methods that are sensitive enough to provide reliable data for nanosized particles [17]. Though it often is more time consuming than ensemble measurements, it is of great importance to consider particles' individual composition to ensure production of nanoparticles with high performance, are reproducible, and attractive for industrial applications [18][19][20]. A concrete example where the individual particle composition is important is when growing high quality nanowires; by adding a certain amount of aluminium to gold nanoparticles, growth of sharp interfaces in Si-Ge nanowires is enabled, something that is essential for electronics such as field effect transistors and quantum dots [21]. Another example involves particles with catalytic behaviour. Depending on the Au/Pt composition ratio, the nanoparticles have shown to exhibit varying catalytic activity, allowing for tuning of the particles properties to best enhance a certain reaction [22].

Despite the above argued importance of the composition of nanoparticles, there are still reports being published where analysis of individual particle composition is neglected [7][13][14][23] [24]. In cases where single particle composition analysis is conducted, it is often not described how the measurements are done, for instance, how many single particles that have been analyzed [12][25]. In other cases, the number of particles analyzed are too few to give a statistically significant result for the entire specimen [26], or the intention is merely to confirm mixing of materials in the particles [7].

1.4 Disposition of Thesis

In the following chapter, theory behind the spark ablation technique as well as how one can control the properties of the resulting particles are presented. Electron microscopy, both in scanning and transmission mode, was used to characterize the nanoparticles, and therefore the basic theory of electron microscopy is explained. For compositional analysis, energy dispersive spectroscopy and X-ray diffraction were used and their principles are briefly explained. Chapter 3 presents the method and experimental setup for the particle generation and following analysis. The results are presented in chapter 4 and are discussed in chapter 5. In the last and final chapter, the main conclusions are presented along with possible future research on the topic.

2 Theory

Below, the basic theory and principles of the techniques used for this project are presented. The chapter begins with an explanation of spark ablation and the spark discharge system, followed by the theory behind the methods used to analyze the produced particles. These analysis methods include Electron Microscopy, X-ray diffraction, and Energy Dispersive Spectroscopy (EDS).

2.1 The Spark Discharge System

To produce nanoparticles using the spark ablation principle, one needs an apparatus consisting of two components; a chamber with electrodes and an electric circuit, together often called the spark discharge generator (SDG). In the chamber, a spark between two electrodes, charged by the electric circuit, occurs and results in nanoparticles. An inert carrier gas, e.g., nitrogen, hydrogen, or argon, is often used to transport the particles away from the electrodes and chamber after the generation.

In order to manipulate or characterize the particles, e.g., size select or sinter them, the SDG is often accompanied by other components placed further down the stream. An example of such a spark discharge system arrangement, and the setup used in this project, can be seen in figure 4 below. The spark discharge generator, "chamber" in the figure below, is followed by a neutralizer, a tandem differential mobility analyzer (DMA) setup, "DMA1" and "DMA2" in the figure, a furnace, an electrostatic precipitator (ESP) and an electrometer. More information about these components can be found in section 2.1.4 below. A pumping system ensures a stable flow of the aerosol and using valves, one can choose to bypass different parts of the system if preferred [27].

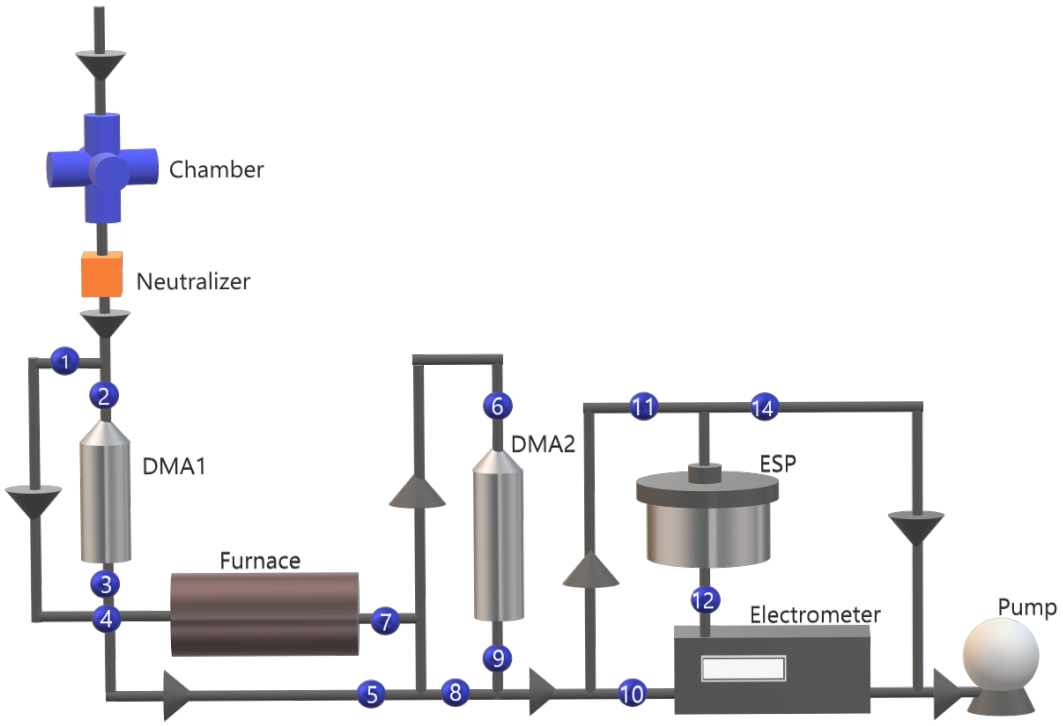

Figure 4: *A schematic of a spark discharge generator (here "Chamber") and following system set-up that allows for manipulation and characterization of the particles. Valves 1-14 can be used to bypass certain components, e.g., by opening valve 1 and 4, and closing 2 and 3, one bypasses DMA1.*

2.1.1 The Chamber & Electrodes

The first essential component for particle generation by spark discharge, the chamber, can have different geometries depending on setup but usually houses two opposing electrodes with a millimeter gap between them. It often consists of intersecting cylinders, allowing for connection of in- and outlet for a carrier gas, two opposing electrodes, and a see-through window, see figure 5.

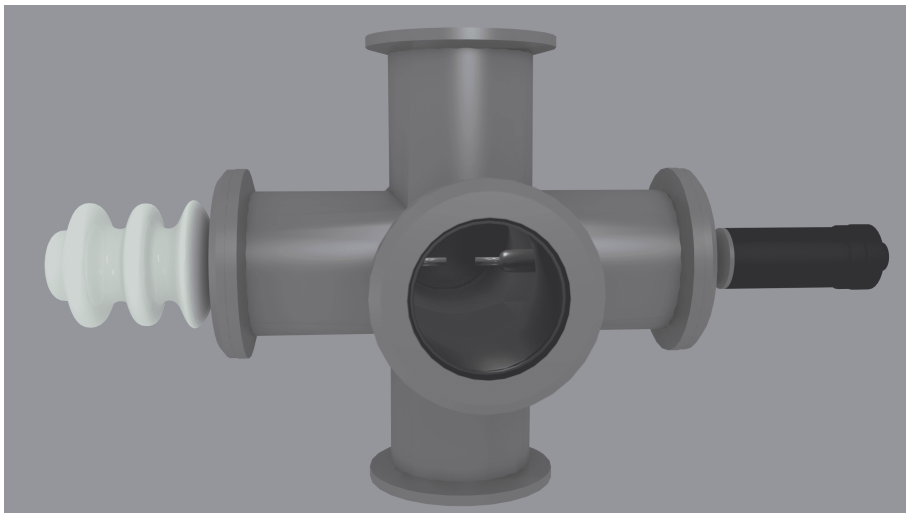

Figure 5: *Example of a spark discharge generator. The electrode holders are here white and black and hold the, just visible, electrodes in place inside the chamber. Figure courtesy of the engineered nanoparticle group at NanoLund.*

Electrodes are often a few millimeters in diameter, 3 mm being the most commonly used in the system used for this project. The electrodes often have a length of a few centimeters, making it easy to fasten them in dedicated electrode holders. As previously mentioned in chapter 1, the electrodes can be made of any conducting or semiconducting material. The reason for this will be more apparent in the following section. It was also mentioned that there are a few ways to produce mixed nanoparticles, and all involve the electrodes. The first method is to use alloyed electrodes, see figure 6a) below. The second way, depicted in figure 6b), which is especially good if the materials used are immiscible as a bulk system, is to use electrodes of two different materials. The third way is also a possible method to use when the intended materials are immiscible in bulk. Here the materials are grinded into micrometer-sized particle powders, then mixed, pressed and sintered together into an electrode shape [2], see figure 6c). Due to a relatively large grain size compared to the ablated area, the chance of the spark to only evaporate one material is quite high, leading to large compositional variation between the particles. The following section will describe the main features and principles of the particle generation mechanism, namely, the spark!

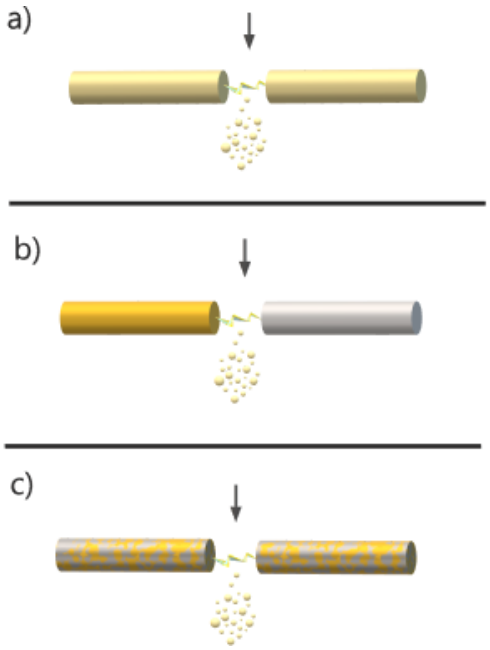

Figure 6: *Schematic figure of how to generate mixed nanoparticles by spark ablation. a) Alloyed electrodes. b) Electrodes of different materials. c) Mixed electrodes of pressed and sintered powder. Picture developed from [2].*

2.1.2 The Spark & Electric Circuit

The second component needed to produce particles with spark ablation, and also the easiest way to control the spark characteristics, is the electrical circuit. The circuit can vary between setups, but is always equipped with a capacitance, an inductance and a resistance, and can be modeled as a simple resistance, capacitance, and inductance (RCL) circuit. Here the inductance arises from the cabling and the resistance from the electrode gap, see figure 7 below. To provide energy for the spark, a high voltage generator is often connected and used to charge the capacitor.

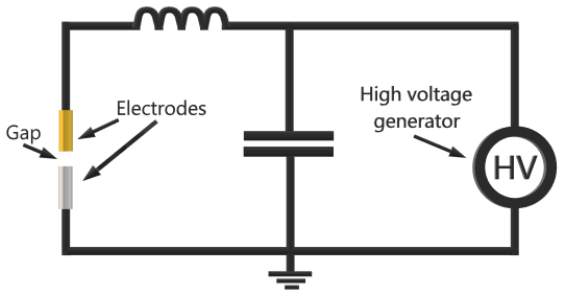

Figure 7: *The electrical system can be modeled as a simple RCL circuit. Picture adapted from [27].*

By charging the capacitor, a voltage is applied across the electrode gap, and when the voltage is high enough, a spark is produced between the electrodes and a brief flow of current occurs. This is the reason why the electrodes must be conducting or semiconducting: a current has to be able to flow through the electrodes. The impact and heat of the spark evaporate and ablate a small amount of electrode material. As it is transported away with the carrier gas, it is allowed to cool, and an aerosol forms [27].

For a spark discharge to occur across the electrode gap, a conductive plasma channel is needed. A high electric field can be accomplished by charging the electrodes with a high voltage source, and allows for a plasma to occur. In the high electric field, molecules and atoms of the carrier gas are ionized, and ejected electrons and cations are accelerated to a high energy. If the energy is high enough, the electrons and cations can, in turn, knock out more electrons from other gas molecules, resulting in an avalanche of charged particles and the formation of a conducting plasma channel. The plasma channel between the electrodes allows for a current of electrons to carry charge across the electrode gap, and a spark discharge occurs [27]. The spark lasts for a few microseconds [2] and the temperature in the electrode gap can reach between 20 000 and 30 000 K.

As previously mentioned, the spark discharge leads to evaporation of electrode material(s) and the volume between the two electrodes will supersaturate. The carrier gas transports the plume of evaporated material away from the plasma vicinity, leading to rapid cooling of the gas and the condensation of tiny particles. The nucleation of stable particles is possible due to adiabatic expansion of the supersaturated gas cloud, radiation, and thermal conduction below the evaporation temperature [27].

There are a few critical parameters that determine the nature of the spark and thus the particle formation. The first is the breakdown voltage V_b of the gas in between the electrodes, and its dependence is shown in equation 1 below:

$$V_b = \frac{Bpd}{ln\left(\frac{Apd}{ln(1+1/\gamma)}\right)} \tag{1}$$

Here B and A are constants, p the pressure, d the distance between the electrodes, and γ the Townsend secondary ionization coefficient. Both B, A and γ are material dependent and vary between different gases. The breakdown voltage V_b of the gas is often not equal to the discharge voltage, V_d, which is the voltage when the spark occurs. The reason for this is that the discharge conditions require some time to develop [28] and the discharge voltage can be expressed as 2:

$$V_d = V_b + V_o \tag{2}$$

where V_o is the overvoltage. How often the discharge occurs, the spark frequency f, is determined by the discharge voltage V_d, the current I, and the capacitance C as in equation 3:

$$f = \frac{I}{CV_d} \tag{3}$$

The spark energy E, is just as the spark frequency, also dependent on the discharge voltage V_d and the capacitance C, however in another configuration, see equation 4 below:

$$E = \frac{1}{2}CV_d^2 \tag{4}$$

The energy per spark (E) influences the amount of material yielded by the spark discharge generator during operation; the higher energy per spark, the more electrode material can be evaporated.

An interesting characteristic of the spark discharge resulting from the electric circuit, is that the

discharge voltage oscillates between positive and negative polarity, see figure 8 below.

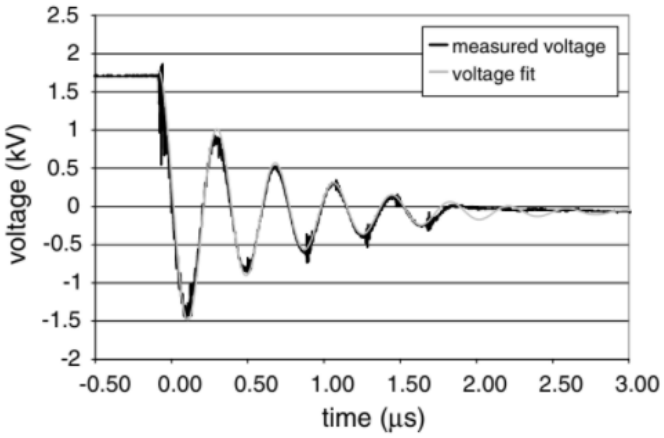

Figure 8: *Typical plot of the oscillating discharge voltage between the electrodes. A model of the damped oscillation shows a good fit to the measured discharge voltage. Figure taken from [28].*

This oscillation can go on for the entire duration of the spark, depending on the damping τ of the system, which can be expressed as below, indicating that the damping can be influenced by changing the resistance of the electrode gap R_{spark} and the inductance of the circuit L_C.

$$\tau = \frac{2L_C}{R_{spark}} \tag{5}$$

The polarity change of the discharge voltage is of high importance for generating bimetallic aerosols using two different electrodes. When the plasma channel is formed, ions and electrons bombard the electrodes and due to the larger mass of the cations than the electrons, the negatively charged electrode is expected to ablate more strongly than the positively charged anode. The change in polarity helps to counteract this effect [27]. There are also reports showing that it is possible to control the amount of material ablated from each electrode by adding an extra resistor to the serial circuit, thereby controlling the damping coefficient and so the amount of material ablated from each electrode [29].

2.1.3 Particle formation

Each spark that occurs in the chamber produces a small vapor cloud that is mixed into an inert carrier gas flow. The cooling associated with the rapid mixing leads to nucleation of primary particles, consisting of atomic clusters up to a few nanometers in diameter, depending on operating conditions. A high number concentration of the primary particles leads to collisions which either can result in complete coalescence, or partly coalescence, commonly referred to as particle necking, see figure 9 below. On rare occasions, particles larger than 50 nm are ablated from an electrode, a phenomenon referred to as splashing. Splashing is thought to arise due to the spark hitting the same area on an electrode multiple times, ablating droplets of electrode material from areas of liquid pools on the surface. Typically the splashed particles only constitute a small portion of the produced particle mass [2].

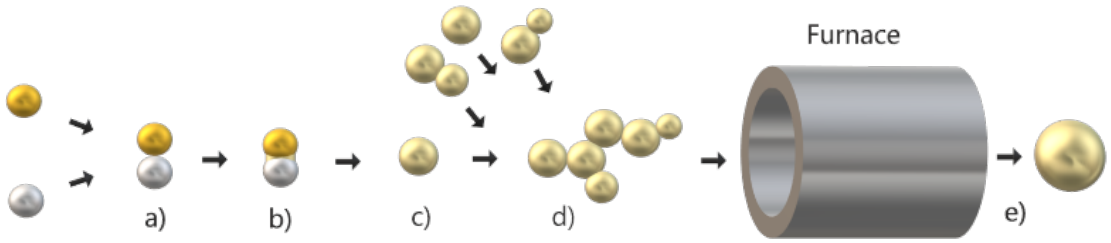

Figure 9: *Early stages of particle growth and following compaction in a furnace. a) collision, b) necking, c) coalescence, d) agglomeration, and e) compaction through sintering. Picture adapted from [28].*

The particle temperature plays an important role in the fate of the colliding particles. In the initial phase of particle formation when the temperature is high, coalescence occurs fast and results in spherical particles. If the temperature is lower, coalescence is slower and necking occurs, resulting in non-spherical particles. As more groups of primary particles collide, with only partial coalescence, agglomerates are formed.

In general, different materials are ablated with different rates depending on material constants like boiling points, evaporation enthalpies, and heat capacities [2]. Therefore, when using two different electrodes, even if the spark oscillation is tuned so that equal amounts of energy is delivered to each electrode, the mass loss from the electrodes will not be equal. The resulting particles will hence contain more of the electrode material which was ablated more easily.

There are a few parameters known to influence the generated particles' properties, e.g., their size distribution and composition, when electrodes of two different materials are used, apart from the electrode material. Some examples are the energy per spark and gap distance, the carrier gas and pressure, and the capacitance and spark frequency [28].

A model developed for producing mixed nanoparticles with spark ablation using two different electrodes is described in [4] and [2]. Here it is assumed that the spark only ablates material from the electrode of momentarily negative polarity, which changes with the oscillation of the spark discharge. It is also assumed that a plume of material is produced in the vicinity of the ablated negative electrode, and this is where the initial stage of particle growth takes place and therefore only consists of initial particles of one pure electrode material. Eventually, diffusion and turbulent mixing of the plumes result in coalescence of pure initial particles from both electrodes, and mixed final particles are produced, see figure 10 below.

Figure 10: *A model of mixed particle formation. Pure initial particles are formed near the two electrodes and are subsequently diluted and randomly mixed, resulting in final particles. Picture taken from [2].*

According to the mixing theory, a few parameters can influence the particle growth and affect the compositional standard deviation of individual particles. It should be mentioned that the report partly bases its experimental results on EDS analysis of (only!) 6-7 individual particles, to support the model predictions. However, the model can be used as comparison to the results obtained in this project, and hopefully lead to a valuable discussion.

The resulting relations of the mixing model can be seen in equation 6 and 7 below. It is assumed that the fraction of one component in the final particles, e.g., the weight fraction of Au, can be described by Poisson statistics and that the composition distribution $f(\varphi)$ then can be approximated by Sterling's formula shown in equation 6:

$$f(\varphi) = exp\left(- \frac{(\varphi - \overline{\varphi})^2}{2\sigma^2} \right) \cdot const \tag{6}$$

Here φ is the particle composition, $\overline{\varphi}$ the mean particle composition, and *const* some constant. The standard deviation σ in equation 7 is here given by:

$$\sigma = \sqrt{\frac{\overline{\varphi}(1 - \overline{\varphi})}{\left(\frac{D_{pf}}{D_{pi}}\right)}} \tag{7}$$

The standard deviation can be influenced by the initial particle diameter D_{pi}, the final particle diameter D_{pf}, and the mean particle composition. From equation 7, there are three ways to decrease the standard deviation. One way is to produce particles consisting of one dominating species, avoiding the maxima (0.5) of $\overline{\varphi}(1 - \overline{\varphi})$. Another way is to increase the final particle diameter, and finally, the last way is to decrease the initial particle diameter [4].

In the developed model, the mean composition is described by both the parameters of the electric circuit, and the electrodes' material characteristics. Consequently, there are many ways to influence the mean composition and the standard deviation. The report highlights a few main effects that should have an influence on the standard deviation: The initial particle size is thought to increase by using a larger separation between the electrodes, thereby increasing the time of pure particle growth before mixing with the other material, resulting in a higher standard deviation. Furthermore, the theory states that more turbulent mixing in the vicinity of the spark, a lower spark energy, or an increase in the carrier gas flow rate should decrease the initial particle diameter, and so reduce the standard deviation. A way to increase the final particle diameter, and reduce the standard deviation, is to control the particle temperature during the production and surface state. Both factors influence the coalescence and growth of particles in the later growth stage.

2.1.4 Beyond the Chamber

Before collection or deposition of the produced particles, they are often already characterized to some extent in the gas phase, and this is referred to as *online characterization* [2]. Advantages with online characterization is that deposition is not needed, and the particles are characterized during production, making it possible to fine tune some of the particles' properties and obtain the preferred characteristics. An example of a spark ablation system was depicted in figure 4, and

below the different components and their function are briefly presented.

The Neutralizer
Due to the presence of electrons and ions in the plasma, the produced particles often obtain charge during the synthesis process. The neutralizer establishes an equilibrium charge distribution of all particles, making it possible to count and obtain a size distribution of all particles [28].

The Differential Mobility Analyzer
In order to measure the size of the produced particles, a differential mobility analyzer (DMA) can be used, and the particles are assumed to have one charge each. A typical setup of a DMA can be described as two concentrically cylindrical electrodes with an air gap between the walls. A potential is applied between the electrodes and as an aerosol flow containing charged particles is introduced close to one electrode, the electric field causes the particles to move towards the other electrode. The particles' trajectories are determined by their electrical mobility, which is related to their size [30]. In this way, the DMA can choose what particle size to let through to the rest of the system. Using two DMAs in a single setup, one can obtain particles with a small size distribution, which often is desirable.

The Furnace
Sometimes, it is preferred to use a sintering furnace in the production setup to reshape the agglomerates into spherical, compact particles. The temperature needed for total compaction differs depending on particle material and size of the agglomerates. In general, the smaller the particle, the lower temperature is needed for compaction. 20 nm agglomerates of Au will compact at around 500 degrees ℃, while Ag has a lower compaction temperature of around 430 degrees ℃[31].

The Electrostatic Precipitator
In order to deposit the produced particles, an electrostatic precipitator (ESP) is used. The operation principle is based on the attraction of charged particles onto an oppositely charged collector. Often, a silicon wafer is placed on a charged plate which helps to attract particles onto the wafer. The wafer with the deposited particles can then be moved and characterized using, for instance, an electron microscope [32].

The Electrometer
An aerosol electrometer provides accurate measurements of the electrical current and flow rate of charged particles with sizes ranging from a few nanometers to a few micrometers. A filter collects charged particles, and a sensitive electrometer measures the current coming from the filter, which can be used to calculate the total number of particles in the aerosol [33].

2.2 Electron Microscopy

Online characterization of spark ablated particles is highly advantageous for several reasons, two of the main ones being that it is simple and does not affect the particles. However, some kinds of detailed information, e.g., the morphology and composition, is very complicated to obtain using online measurements, and can instead be provided in very simple ways using *offline characterization*.

In offline analysis, the particles must be deposited or collected in some way, and this often includes exposing the particles to a different gas atmosphere than the one in which they were produced, which in some cases can affect their properties. One of the most common techniques for offline characterization of spark generated particles is electron microscopy (EM). This technique can provide information about both the morphology and composition, even for particles around 1 nm in size [2]. In this section, both scanning electron microscopy (SEM) and transmission electron microscopy (TEM), two of the most used EM techniques for characterizing spark ablated nanoparticles, will be covered. An advantage with EM is the capability to analyze both individual particles, as well as obtaining an overview of a large number of particles.

Using Electrons to See

Why do we use electrons to see? Well, this has to do with resolution. Resolution is defined as the smallest distance between two separate points we can see, before they look like a single point. Using only our eyes, this distance is about 0,1-0,2 mm, and therefore we say that our eyes' resolution is about 0,2 mm. The image resolution, δ can approximately be expressed using Rayleigh's criterion for light microscopy:

$$\delta = \frac{0.61\lambda}{\mu sin\beta} \tag{8}$$

Here λ is the wavelength of the radiation, μ the refractive index of the viewing medium, and β the semi angle of collection of the magnifying lens. $\mu sin\beta$, often called the numerical aperture, can for simplicity be approximated to 1, making the resolution about half of the wavelength. It is now clear that the shorter the wavelength, the better the resolution is. Green light has a wavelength of about 550 nm, limiting the achievable resolution in a light microscope to about 300 nm. In many cases, e.g., when examining a living cell with a diameter of 2 μm, this resolution is enough. However, to be able to resolve materials' structure on the atomic and nanometer level, this resolution is not enough [17], and other methods to improve the resolution have to be used.

In the beginning of the 20th century, the limit of light microscopy was well understood, and it was not before de Broglie's famous equation relating electrons' wavelength to their momentum, that the resolution problem could be solved. Ignoring relativistic effects, it can be shown that for electrons:

$$\lambda = \frac{1,22}{\sqrt{E}} \tag{9}$$

Here the wavelength is in the unit nm and the accelerating voltage is in the unit V. The equation describes a very useful relation; by increasing the energy, or accelerating voltage, one can decrease the wavelength of the electrons [17]. Most EMs use accelerating voltages between 1 and 300 kV, giving theoretical resolutions of 0,004 nm, much smaller than the diameter of an atom ($\sim$ 0,1 nm). However, imperfect electron lenses make it impossible to achieve the theoretical resolution limit, and instead the resolution is about 2-0,2 nm, depending on the microscope [17]. In an EM, electrons are accelerated onto a sample with which they interact with in the so-called interaction volume, and the result is many different signals, see figure 11 below. The figure shows how the electron beam penetrates the sample and what different signals one can obtain as a result from the interaction. When detected, the signals provide various information about the sample. Photons from the sample contain information about the composition and this is made use of in Energy-

Dispersive X-ray Spectroscopy (EDS). Signals from escaping surface electrons are used in SEM to get valuable topological structure information. If the sample is thin enough, the incoming electrons can go through the sample, transmitted to the other side. These electrons are utilized in TEM and can provide information about the crystal structure, e.g., how the atoms are arranged in the sample.

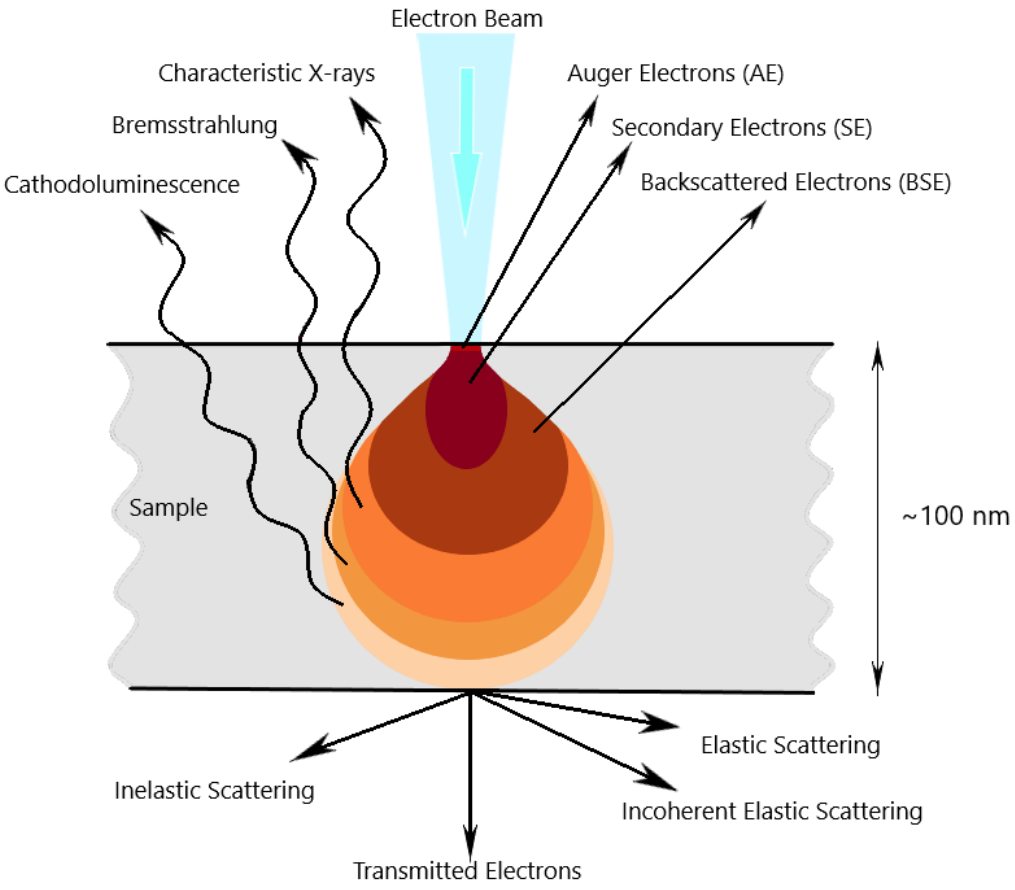

Figure 11: *Signals from different parts of the interaction volume, here depicted in 2D, of a sample when bombarded with high energetic electrons. Figure developed from [34].*

In the following two sections, the principles, possibilities and limits of SEM and TEM are described. Both types of EMs are often equipped with photon detectors, enabling EDS as an important complement for the sample analysis. The EDS technique is described in section 2.3.

2.2.1 Scanning Electron Microscopy

In a SEM, a highly energetic electron beam is, as the name suggests, scanned over a specimen to produce signals that can be detected and interpreted in order to form an image of the sample surface. A SEM is often used to provide an overview of a sample, but can also be utilized to examine small features with a typical resolution between 1 and 20 nm [2].

As the electron beam hits the surface, electrons penetrate the sample and interact with the sample atoms either elastically, i.e., they don't lose any energy, or inelasticity, i.e., they lose a part of their energy to the specimen. The higher energy the beam electrons have, the deeper into the specimen

they can travel and still produce a detectable signal at the sample surface, and the larger the interaction volume becomes. Depending on the nature of the interaction between the electrons and the sample atoms, different signals are produced. Some examples of detectable signals are secondary electrons (SEs), backscattered electrons (BSEs) and characteristic X-rays. Photons are generated from the entire interaction volume, and so are the electrons. However, electrons have a hard time escaping the sample if generated deep into the sample, and therefore, detected electrons at the surface tend to originate from the upper part of the interaction volume, see figure 11.

To create a SEM image, the SE and/or BSE signals are detected, and used to build an intensity distribution map. This results in a 3D image of the sample surface, often, but not always, easy for the human mind to interpret. The SE signal arises when the beam electrons inelastically knock out k-shell electrons from the specimen atoms, and often originates from the top few nanometers. This signal results in a high-resolution image of the surface topography, compared to the BSE signal which can originate from deeper within the specimen. The BSE signal consists of beam electrons that have interacted elastically with the specimen atoms and scattered backwards to the sample surface again. Hence, the BSEs have a higher energy than the SE. An advantage with BSEs is that they can provide chemical information of the sample, due to the fact that heavier elements scatter the electrons more than light elements. This results in an image of the sample where brighter and darker areas correspond to the lighter and heavier elements, respectively. [17]

The magnification of a SEM image can often be varied from 10 up to more than 500 000 times [2], making it a convenient tool for both overview and detailed analysis of the sample. Figure 12 below highlights the ease of obtaining overview images with the SEM. Drawbacks that to some extent limit the possibilities with conventional SEM is the requirement of a high vacuum environment and that the samples have to be conductive. Beam electrons that cannot escape to the sample surface have to be able to exit through alternative routes, thereby avoiding charging effects that else might reduce the resolution. Spark ablated particles, consisting of non-insulating material(s), do not pose a charging problem for SEM imaging, as long as they are deposited on conducting or semiconducting surfaces, typically a silicon wafer. In figure 13, the schematics of TEM and SEM are depicted. Observe the similarities in the lenses used and the difference in the placement of the sample.

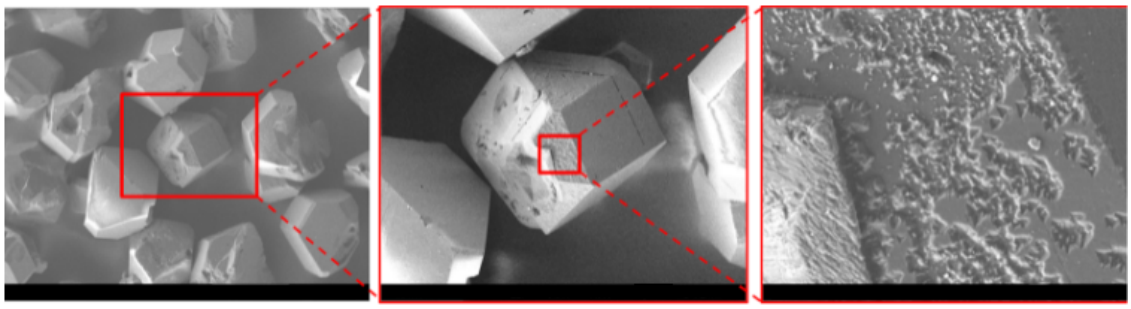

Figure 12: *SEM images of diamond crystals magnified 250 times (left), 600 times (center), and 6000 times (right).*

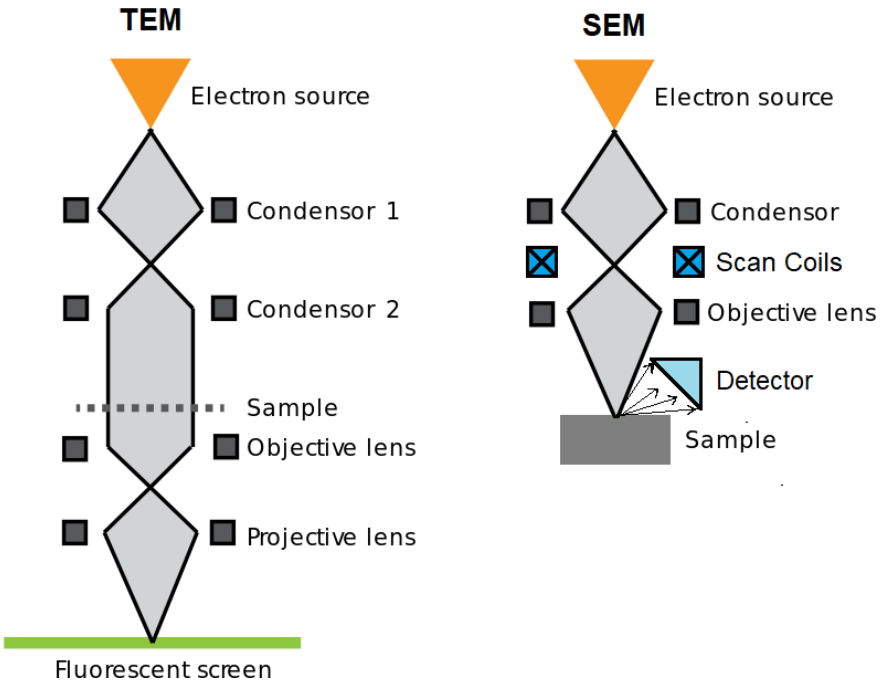

Figure 13: *A schematic overview of conventional TEM and SEM. The electron beam is shown in light grey and the electromagnetic lenses are shown as dark grey squares. Figure developed from [35].*

2.2.2 Transmission Electron Microscopy

To obtain an image of a sample in transmission, it has to be thin, or better expressed, electron transparent. This can mean different things for different materials since it depends on the energy of the electron beam and the mean atomic number of the sample. However, the thinner the better, and one should in general always strive for samples thinner than 100 nm [17]. For spark ablated particles, this is not a problem since they usually are smaller than 20 nm, and not larger than 100 nm in diameter. They merely need to be deposited on a TEM grid and transferred into the TEM sample holder, skipping many tedious and challenging steps typically needed for sample preparation [2].

It is important to remember that a TEM image is a 2D shadow representation of a, typically, 3D sample, which has been averaged over the sample thickness. To fully understand and correctly interpret the image, one needs a good understanding of the interactions between the electrons and the sample, and even then, it can be a challenging task. Other techniques which are depth-sensitive and or surface-sensitive, such as the SEM, should be used as complementary techniques in order to fully understand and characterize a sample. [17]

A TEM can typically be operated in two modes, either in the conventional or in the scanning mode, called scanning transmission electron microscopy (STEM). Some TEMs can work in both modes. The TEM depicted in figure 13 is operated in a conventional mode. Compared to the conventional mode where the beam is parallel when it enters the sample, in the scanning mode, the beam is focused into a small probe which is scanned over the sample just like in a SEM. The STEM mode can be particularly useful when obtaining images of a specific area of the specimen,

or for when an element map of a certain location is required, see figure 14 below where STEM-EDS of a sample is conducted. [2]

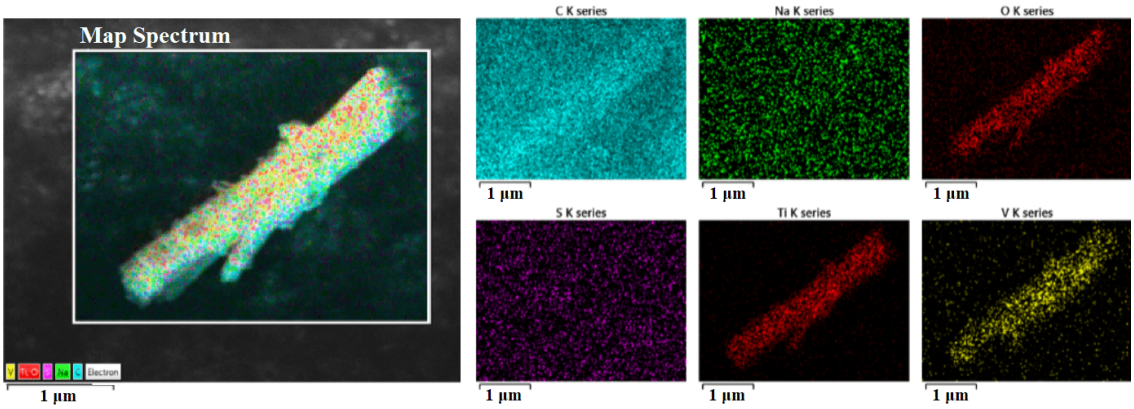

Figure 14: *A STEM-EDS map image of a titanium dioxide nanowire contaminated with vanadium.*

As previously mentioned, electrons entering and interacting with a specimen can either be elastically or inelastically scattered, depending on if there is a transfer of energy or not. The contrast in a TEM image mainly arises from the elastically scattered electrons. Using the wave approach of an electron, stating that the electron wave has both an amplitude and a phase, the occurrence of the contrast can easily be explained. As the electrons transverse the specimen, interactions can change both their amplitude and phase, giving rise to the contrast of a TEM image. Though both contrasts are present in a TEM image, it is often dominated by one type [17].

The interaction between the electron waves and the sample is called *diffraction*, and the *diffraction pattern* is created by the distribution of diffracting electrons that can be found in the *reciprocal space*, see figure 15. The diffraction pattern is directly related to the structure of the sample and can for instance help determine if the specimen is amorphous or crystalline. The TEM is particularly useful for imaging individual crystals due to its ability to determine crystallographic orientations locally, down to the nanometer level [17]. For samples containing many non-oriented crystals of the same kind, e.g., nanoparticles, a technique called powder X-ray diffraction (XRD) can provide average of the crystals' structure by viewing them at the same time [2]. Powder XRD is an important complementary technique to the TEM, but is limited in the sense that it can not provide information about any individual defects or structural differences in the crystals. More detailed information about XRD will be provided in section 2.4.

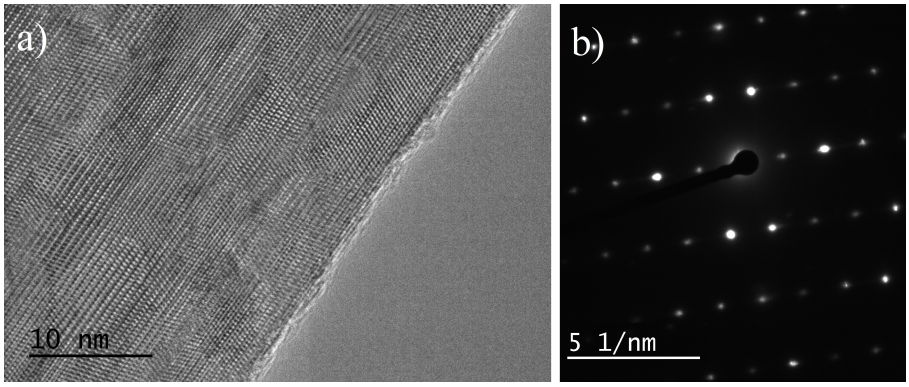

Figure 15: *a) TEM image of the edge of a crystal and b) its diffraction pattern in reciprocal space.*

There are two types of amplitude contrast, mass-thickness and diffraction contrast. Mass-thickness, as the name implies, strongly depends on the density, atomic number and the thickness, and comes from incoherently scattered electrons. In samples that are non-crystalline, e.g., polymers and biological samples, it is the most important contrast contributing to the image [17]. Diffraction contrast comes from coherently scattered electrons and depends on the crystal structure and orientation of the specimen. A major difference between mass-thickness and diffraction contrast, is the importance of selecting scattered electrons to form the image. In an image dominated by mass-thickness contrast, any scattered electrons can be used [17].

The second type of contrast, arising whenever two or more beams contribute to the image, is phase contrast. Though phase contrast is present in most TEM images, even at low magnification, it is considered a high-resolution contrast and the corresponding technique is called high resolution TEM (HRTEM). This is used when detailed information about the atomic structure of thin specimens is needed. The phase contrast is sensitive to many factors: thickness, orientation, and scattering factor of the specimen, not to mention variations in focus and astigmatism of the objective lens. Since phase contrast can be quite difficult to interpret, the technique is often compared with computer simulations to ensure a correct interpretation of the HRTEM images. [17]

Spark ablated particles are often analyzed in a conventional TEM to investigate size, morphology, crystallinity, and mixing. Though some of this information, e.g., size and morphology, can be obtained in a SEM, more accurate measurements are sometimes needed and can be provided by a TEM. The TEM can also help determine if a spark ablated particle is crystalline or consists of a mixed crystal of otherwise immiscible materials. Using a TEM, the chemical composition is usually determined by an accompanying EDS system, or by measuring the lattice distance in a HRTEM image. The latter method is commonly used to prove the existence of an alloy phase in spark ablated particles produced by two different electrodes. [2]

2.3 Energy Dispersive X-ray Spectroscopy

Energy Dispersive X-ray Spectroscopy (EDS, EDX, EDXS or XEDS, here EDS) was developed in the end of the 1960s and in the next decade it was available in many TEMs and even more common in SEMs. The EDS system detects and interprets X-rays to determine what element the

X-rays are originating from and how much of the material that is present in the sample. X-rays are for instance produced when an electron beam hits a material, and hence the good fit for the system within TEM and SEMs. The final output from EDS is a spectra, a plot of X-ray counts, intensity, versus the X-ray energy. Simply put, how many X-rays with certain energies that are detected.

When electrons interact with matter, two kinds of photons can be generated; characteristic X-rays are produced when an atom is ionized, bremsstrahlung X-rays arise when electrons are slowed down as a result of interaction with an atomic nucleus. An EDS spectra consists of characteristic peaks superimposed on a background of bremsstrahlung, the latter generally considered as a nuisance by most material scientists. [17] Figure 16 below shows the process of X-ray emission. A high energy beam electron penetrates the sample and interacts inelastically with an atom's inner core electrons. If more than a certain energy is transferred to the core electron, it can escape the attractive field of the nucleus, leaving the atom ionized, with a hole in the core shell. To return to a lower energy state, an electron from a higher shell can fill the vacancy, an action which is accompanied by either the ejection of an X-ray or an Auger electron. Both processes contain characteristic information about the atom's energy levels which are unique to the element.

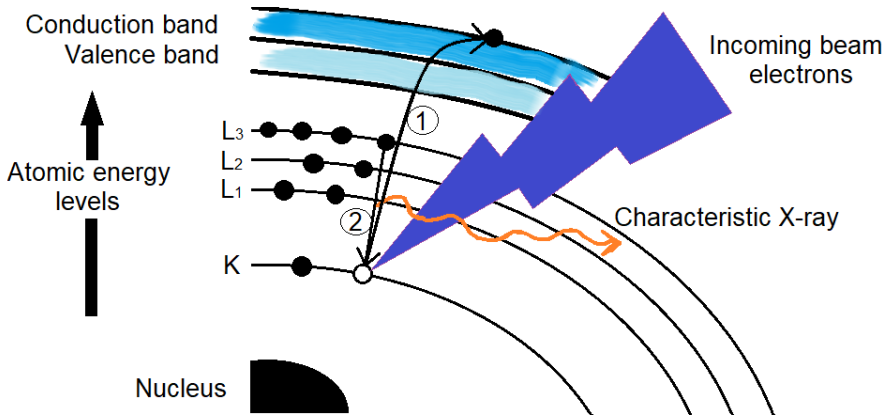

Figure 16: *The ionization process (1) and subsequent emission of a characteristic X-ray (2). A K-shell electron is ejected from the atom by an incoming beam electron. A higher energy L-shell electron fills the hole and emits a characteristic X-ray. Figure developed from [17], page 52.*

As previously mentioned, the second kind of photons generated as the beam electrons interact with the specimen is bremsstrahlung X-rays. Just like the German name suggests, the signal is produced as a result of deceleration, breaking, of an incoming beam electron. This happens if a beam electron penetrates the electron shells and interacts inelastically with the coulomb field of the nucleus. The electron then ejects a bremsstrahlung X-ray with an energy depending on the strength of the interaction, which can be any energy up to the beam energy. The probability of producing bremsstrahlung can be predicted by the atomic number, the incoming electron beam energy, and the deceleration energy. High atomic number, high beam energy and small energy losses generate the most bremsstrahlung X-rays. As previously mentioned, the narrow peaks of characteristic X-rays are superimposed on an continuous bremsstrahlung background which is typically subtracted as it obscures the characteristic lines.

The EDS system consists of three main parts; a detector, processing electronics and a multi-channel

analyzer (MCA) display, and all parts are controlled by a computer [17], see figure 17. The process starts as an X-ray hits the detector which then is identified by the pulse processor. The final signal is stored at the correct energy in the MCA display. In the following section, the function of the EDS system will be explained in more detail. Thereafter the method of quantification of elements is described, and finally some important features to be aware of during spectra analysis will be presented.

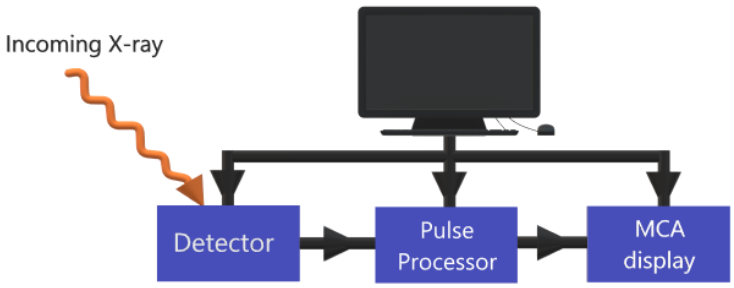

Figure 17: *Diagram over the main parts of the EDS system; the X-ray detector, the pulse processing electronics and the multi channel analyzer display, all controlled by a computer. Figure developed from [17], page 558.*

2.3.1 Function

The EDS process starts with the detector, and an EDS detector is almost always made of a silicon-lithium semiconductor, the detectors used in this project being no exception. As X-rays hit the detector, valence band electrons are given enough energy to be transferred to the conduction band, creating electron-hole pairs in the semiconductor. By applying a bias across the detector, the generated electrons and holes are separated and a charge pulse of electrons can be measured by an ohmic contact. The number of generated electron-hole pairs is directly proportional to the X-ray energy, and can be used to distinguish most elements in the periodic table with good precision with the help of the processing electronics [17].

The mentioned charge pulse of electrons created in the detector enters the processing electronics, and a field effect transistor isolates, amplifies, and converts the charge pulse to a voltage pulse. The signal is then amplified thousands of times and shaped so that it can be recognized as coming from an X-ray of a specific energy by the pulse processor. The computer then assigns it to the appropriate channel in the MCA display, which has a typical resolution of about 10 eV. There are two important variables in the pulse processing electronics that can be controlled, the time constant (τ) and the dead time. The time constant determines for how long the pulse processor evaluates the pulse magnitude, and is typically varied between 10-50 microseconds. By using a larger time constant, the system is better at assigning the right energy to the pulse, but can not process as many counts per second (cps). A smaller time constant allows for faster processing, but with a greater error when assigning the right energy to the pulse. The dead time is the amount of time (in percent) that the detector is switched off after being hit by an X-ray in order to analyze the pulse. As many X-rays enter the detector, the dead time increases, and a too high dead time means that the detector is being swamped by X-rays which makes the collection inefficient. A count rate up to about 10 000 cps is to be expected for a normal detection system [17].

Ideally, the detector system should only process one X-ray at a time, and this is overseen by the computer. When an X-ray signal is detected, the computer makes sure that the detector is switched off so that the signal can be processed by the electronics. The computer also decides the time required to analyze and assign the signal to the correct energy channel in the MCA. Calibration of the spectrum, recording of conditions under which the spectrum is acquired, and any data processing is also governed by the computer software. The speed of the entire process allows for an entire spectrum to be recorded in just a few seconds to a minute, though the longer acquisition time used, the more detailed the spectrum becomes, allowing for easier peak identification and quantification [17].

2.3.2 Quantification

It is crucial to perform qualitative analysis of the specimen before proceeding with any quantitative analysis. Qualitative analysis involves identification of every peak in the spectrum with statistical certainty. Therefore, it is advantageous to acquire spectra with sufficient X-ray counts to draw the right conclusions from the analysis. Though the computer system automatically can identify peaks for you, one should be aware of the process of peak identification as well as common artifacts in the spectra to ensure correct analysis of the specimen. Some artifacts and how to recognize them will be discussed in the analysis section below.

Peak Identification

Typical peak identification involves three steps: Identify the most intense peak and its family, continue to the next most intense peak not included in the previous step and repeat the family search. Continue until all peaks are identified, then think about pathological overlap such as spurious, system and artifact peaks, see section 2.3.3 below. The method should permit identification of all major peaks in the spectrum. However, there might still be small peaks or fluctuations of intensity present which might be significant to identify, or else should be dismissed as noise. Fortunately, there is a simple statistical criterion that can be used to decide if the peak is significant and should be included in the analysis. This involves counting X-rays for a long enough time so that the peaks are visible and the bremsstrahlung intensity is smooth. Then, displaying the peak and background, one should separate the peak intensity (I_A) from its background intensity (I_A^b) and integrate over the same number of energy channels. If $I_A > 3\sqrt{I_A^b}$, then the peak is statistically significant and should be identified. Using this criterion, the identification will be wrong in less than 1% of the time.

In cases where peaks in the spectra overlap, one can try to perform peak deconvolution. There are often standard software routines in EDS computers that are capable of detecting and resolving the most common peak overlaps. One example of a deconvolution is shown in figure 18 below.

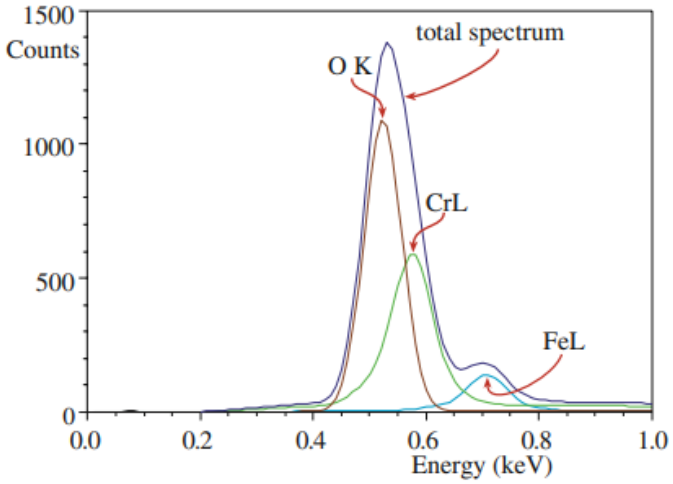

Figure 18: *The total spectrum (dark blue) consists of overlaps of three spectral peaks from a mixed Fe-Cr oxide. Deconvolution of the individual contributions in brown (O K_α), green (Cr L_α), and light blue (Fe L_α) is crucial for intensity determination and following quantification. Figure taken from [17], page 631.*

Element Quantification

Now that we have a spectrum that has been analyzed qualitatively, one can continue with the quantitative analysis of the specimen. The procedure of bulk microanalysis, typically performed by SEM-EDS, is similar as for thin and electron transparent specimens typically analyzed by TEM-EDS. Both are based on Castaing's proposition from 1951, assuming that the concentration C_i of element i generates characteristic X-rays of some intensity I_i [36] [17]. Since it is difficult to measure all the generated intensity, it was proposed to use a standard sample with a known concentration of element i, $C_{(i)}$, and instead measure the intensity ratio $I_i/I_{(i)}$ where $I_{(i)}$ is the measured intensity coming from the specimen:

$$\frac{C_i}{C_{(i)}} = [K]\frac{I_i}{I_{(i)}} \tag{10}$$

K in the expression is called the sensitivity factor, which takes into account and corrects for the difference between generated and measured X-rays for both the standard and the unknown sample. Three effects contribute to the sensitivity factor:

- Z- The atomic number.
- A- Absorption of X-rays within the specimen.
- F- Fluorescence of X-rays within the specimen.

The correction procedure in bulk microanalysis is therefore often called ZAF correction, and can be quite complex which is why it usually is performed by a computer. As previously mentioned, the correction procedure for bulk microanalysis differs from the procedure needed for thin and electron transparent specimens. In this project, the focus has been to perform element analysis using TEM-EDS on individual sparks ablated particles, which classifies as thin specimen EDS analysis. Therefore, ZAF correction for bulk microanalysis will not be further discussed in this report, apart from a short segment about absorption correction in section 2.3.2.

For thin specimens, both absorption A and fluorescence F in the specimen can be ignored due to the small interaction volume, leaving only the atomic number Z to correct for. Further simplification for analysis of thin films was shown by Cliff and Lorimer in 1975. They showed that the intensity from a standard was not needed, and instead one could simply measure the ratio of the intensities from two different elements in the same sample. Using the so-called Cliff-Lorimer equation, it is possible to relate the weight percentages, C_A & C_B of two elements (A & B) to their measured intensities, I_A & I_B:

$$\frac{C_A}{C_B} = k_{AB}\frac{I_A}{I_B} \tag{11}$$

Here the term k_{AB} is called the Cliff-Lorimer factor and varies depending on the acceleration voltage and the TEM/EDS system used. k_{AB} is also related to the atomic number correction factor Z. In order to obtain absolute values for C_A and C_B, one can assume that the sample is a binary system and hence:

$$C_A + C_B = 100\% \tag{12}$$

A similar relation can be applied to ternary and higher systems by using extra equations like:

$$\frac{C_B}{C_C} = k_{BC}\frac{I_B}{I_C} \tag{13}$$

and

$$C_A + C_B + C_C = 100\% \tag{14}$$

The k-factors for different pair of elements analyzed under the same conditions are related as:

$$k_{AB} = \frac{k_{AC}}{k_{BC}} \tag{15}$$

To summarize, in order to quantify the elements in a spectrum, one has to determine a value for the k-factor and measure the peak intensities. For the intensities, one should try to only use the K_α lines. The L or M lines can also be used, though they often are more difficult to resolve. L-lines, and in some cases M-lines, have been used for quantification of Ag and Au in this project since the K_α peaks have higher energies than what is detected by the EDS-system, and are therefore not visible in the obtained spectra. To determine the peak intensities one has to remove the background intensity before intensity integration can be performed.

Background Subtraction

When a spectrum for quantitative EDS analysis with high enough counts in the characteristic peaks is obtained, one can remove the background and then measure the peak intensities. There are several ways to perform background subtraction to a spectra, and the best approach depends on what the spectra looks like. Some methods are better for when the characteristic peaks are in the low-energy regime, others depend on whether the peaks are isolated or close together. The most simple method of estimating the background contribution to a characteristic peak is the window method, see figure 19 below.

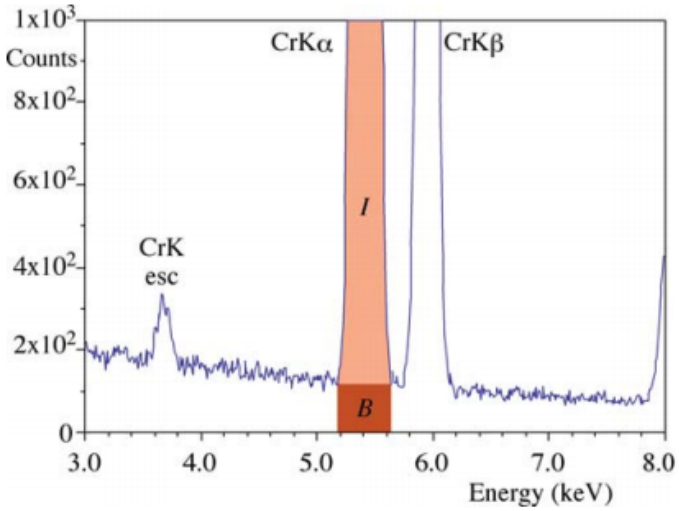

Figure 19: *Illustration of the window method for background (B) subtraction to the intensity (I) of a characteristic peak. Figure taken from [17], page 642.*

The window method can be used when isolated characteristic peaks are superimposed on a slowly varying background intensity. By drawing a line across the peak that divides it from the peak background, a "window" is created. The window has the same width as the peak and can be subtracted to the integrated peak intensity. If the spectrum consists of overlapping peaks or if they lie in the low energy regime where the background intensity changes rapidly, more sophisticated methods are needed. One such method is to model the background. Using a mathematical model, one can produce a smooth curve-fit of the background spectrum and then subtract it which is particularly useful when many peaks are present and there is little space for estimations using the window method.

Peak Intensity Integration

Now that the background intensity below the peaks are estimated and subtracted from the spectrum, one can integrate the peak intensities. The integration is done in different ways depending on the method used for background subtraction. If a window method was used for background subtraction, the peak intensity (I) is obtained by subtracting the estimated background (B) to the total intensity (I+B) in the chosen window, see figure 19 above. If the background was subtracted by mathematical modeling, the peak intensity is often obtained by letting a computer fit a slightly modified Gaussian to the peak and then integrate to get the total number of counts in the energy channels [17].

Determination of k-factors

k-factors are almost never the same between two microscopes. The only condition when it can be expected to be the same for different microscopes is when using the same standard, the same accelerating voltage, same detector configuration, and the same background subtraction and peak integration methods. To determine k-factors one can either use an experimental determination approach using standard samples, or simply calculate them using a theoretical approach. The latter approach is less reliable, though fast and easy compared to experimental determination. Even if one uses the experimental approach, the error of k_{AB} is difficult to reduce to $\pm$ 1%, and

this error must in turn be added to errors in measurement of the intensities [17]. This should be considered when quantitative data is presented.

Calculation of k-factors is useful when the accuracy is less important and a fast indication is preferred. An expression for the k-factor for atomic weight (A_A and A_B) quantification of element A and B can be seen below:

$$k_{AB} = \frac{1}{Z} = \frac{(Q\omega a)_A}{(Q\omega a)_B} \frac{A_B}{A_A} \frac{\varepsilon_A}{\varepsilon_B} \tag{16}$$

As previously mentioned, the k-factor is related to Z, the atomic number correction factor. Q is the ionization cross section of an atom, ω is the fluorescence yield for characteristic X-rays, a is the relative transition probability of an electron to a certain atomic shell, and ε the detector efficiency. The k-factor is dependent on the accelerating voltage (affects Q), the atomic number (affects ω, A and a), and the method for peak integration (affects a), not to mention the detector used (affects ε).

The AZtec software used for peak identification, background subtraction, k-factor determination and element quantification in this project uses a combination of algorithms collectively called TRU-Q. The technique provides quantitative results with an accuracy only previously achieved using well characterised and closely matched standard materials [37]. Except for the calculated weight and atomic percentages of the elements present in the analysed specimen, the AZtec software can show what k-factor and what absorption correction factor it has used for the quantification, if the user is interested.

Absorption Correction

The Cliff-Lorimer equation assumes that the specimen is thin enough that both absorption and fluorescence in the sample can be ignored. This is, however, not always the case, especially for bulk specimens. The X-ray absorption correction is usually the largest factor that has to be considered for measurement of the element composition in bulk microanalysis [36]. The problem with absorption effects is that X-rays from one element in the specimen might be preferentially absorbed by the specimen, meaning that the detected intensity counts from that element will be less than the generated intensity. A result is that C_A no longer is proportional to I_A. This can occur if the specimen is too thick, the characteristic X-rays come from light elements (energy below 1-2 keV), or when the spectrum contains X-ray lines from both light and heavy elements that have different probabilities of being absorbed. To account for preferential absorption, the following expression, 17, for the effective sensitivity factor k^*_{AB} can be used:

$$k^*_{AB} = k_{AB}(ACF) \tag{17}$$

Here ACF is the absorption-correction factor, and depends on the depth distribution of generated X-rays in the specimen. This in turn depends on the sample thickness t and density p. The ACF factor is unity when no absorption occurs. In equation 17 above, it is assumed that the X-ray generation is constant through the specimen, but the ACF factor still depends on the thickness and density of the specimen.

The density depends on the composition, and therefore, the absorption-correction procedure is an iterative process where the first step is to use the Cliff-Lorimer equation without absorption

correction. From the obtained C_A and C_B values the computer can then calculate a value for the density, and then new values for the composition and so on. The calculation often converges after two or three iterations. In this project the AZtec software has been used, in which it is possible to insert values for both the thickness and the density of the specimen, if it is approximately known. The software can then start the iteration from those given values. The signal from Ag is expected to be absorbed more strongly than from Au, and therefore Ag has a higher absorption coefficient than Au.

2.3.3 Analysis

As mentioned in the previous section, one has to be aware of common artifacts in the spectrum introduced by the EDS system. The EDS artifacts can be divided into two groups; signal-detection artifacts, and signal-processing artifacts. In addition, one has to be wary of so-called system and spurious X-rays originating from the illumination system and parts of the specimen not intended for analysis. These artifacts can be divided into pre-specimen effects and post-specimen scatter (in the case of TEM-EDS), and one should be aware of how to take appropriate precautions to identify and minimize the problems caused by them.

EDS System Artifacts

To the signal-detection artifacts belong escape peaks and internal-fluorescence peaks. Escape peaks arise due to the fact that the detector is not perfect in detecting all the energy of an X-ray. While most energy is transformed into electron-hole pairs, some energy might be lost. The most common reason for losing energy is if an incoming photon fluoresces a Si K_α X-ray with energy 1,74 keV which escapes from the detection region of the detector. The detector then registers a photon energy of E−1,74 keV. Therefore, Si escape peaks appear 1,74 keV below the true characteristic peak in the spectrum. Typically, escape peaks only appear if there are major characteristic peaks in the spectrum, otherwise they will not be large enough to be distinguished. The analysis software should be able to both recognize, remove and add the intensity from the escape peak back to the characteristic peak where it originates.

A large characteristic peak from Cu is expected for TEM-EDS due to the use of a TEM Cu-grid for imaging and analyzing the particles in transmission mode. Therefore, monitoring of possible escape peaks 1,74 keV below the Cu characteristic peak will be relevant. In SEM-EDS a major characteristic peak from Si is expected, coming from the fact that the wafer, onto which the particles are deposited, is made of Si and its oxide.

Internal-fluorescence peaks are characteristic peaks from the detector, typically from Si in silicon-lithium semiconductor detectors. Photons can fluoresce Si-atoms in the detector and result in Si K_α X-rays which are detected and registered as a small peak in the spectrum. Depending on the design of the detector, the Si artifact signal can have an intensity of about 0,1% to 1% of the specimen composition, so it is not a major problem, but one should be aware of it. The detectors used for both SEM-EDS and TEM-EDS in this project are, as previously mentioned, silicon-lithium detectors, and an internal fluorescence peak from Si is to be expected. Another possible internal fluorescence peak can come from the ohmic contacts of the detector, which are made of Au. This signal is sometimes detectable as a small disturbance in the bremsstrahlung

intensity but its effect on microanalysis is negligible.[17]

A signal-processing artifact is the occurrence of sumpeaks. This phenomenon arises when two X-rays enter the detector at almost exactly the same time, and the electronics are not fast enough to switch off the detector and hence only detect the first X-ray. Then the sum energy of the two incoming photons is registered by the analyzer and results in a sum peak in the spectrum. The event is more likely to happen for the X-rays from a major peak, so the sum peak (or double peak) often appears at twice the energy of a major peak. Some conditions when one should be wary of sum peaks is when the input count rate is high, the dead time is higher than about 60% and when there are major characteristic peaks in the spectrum. Sumpeaks rarely constitute a problem, except for when analyzing elements lighter than Mg [17]. During the EDS analysis for this project, the count rate and dead time will be monitored and held at normal values (count rate $<$ 10 000 cps and dead time $\sim$20-30 %) in order to suppress artifacts that might arise from too high count rates and dead time. The analysed elements intended for quantification (Ag and Au) are not lighter than Mg, so sumpeaks are not expected.

Illumination System Artifacts

Ideally, all the X-rays detected by the EDS detector should originate from the interaction volume of the specimen, and the only source of radiation on the sample should be the electron beam. However, in practice this is not the case. This fact indicates that the obtained spectrum is not always characteristic only of the intended region of the specimen. One factor that is responsible for the problems is the high acceleration voltage of the electron beam which can lead to generation of X-rays and electrons in the illumination system. Another factor is the scattering of high-energy electrons and X-rays by the specimen.

Pre-specimen effects arise when the illumination system, i.e., column components, produce high-energy bremsstrahlung X-rays and uncollimated electrons which can strike the specimen anywhere. This leads to spurious, i.e., unwanted, X-rays which are indistinguishable from the ones generated in the region of interest, see figure 20 below.

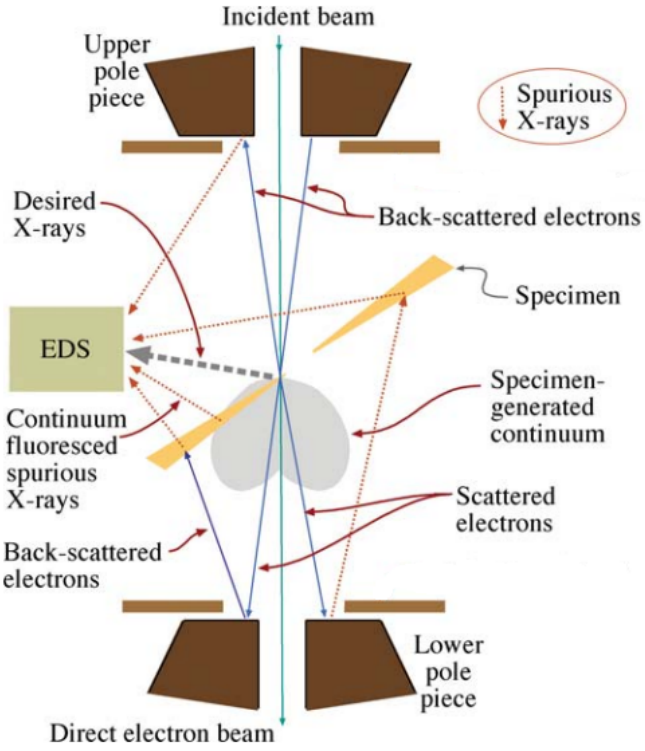

Figure 20: *System and spurious X-rays generated when the electron beam (in green) is scattered by the specimen when analyzed in transmission mode. The thick grey dotted line represents the desired X-rays from the intended region in the sample. Back- and forward scattered electrons (in blue) excite system X-rays in the stage and spurious X-rays from elsewhere in the specimen. The grey region after the sample is the bremsstrahlung continuum that can fluoresce, for instance, the specimen at another spot than the desired, which also generates spurious X-rays. Figure developed from [17], page 611.*

Post-specimen scatter is only relevant for TEM-EDS analysis where the specimen is thin and the electrons are scattered in the forward direction. Most forward scattered electrons are gathered by the imaging system of the microscope. However, some electrons are scattered through high enough angles so that they strike the specimen holder, the pole piece (consisting mainly of Fe and Cu), or some other part of the microscope stage, see figure 20. The electrons may then generate characteristic X-rays of the microscope materials which can be detected by the EDS system. Another possibility is that the X-rays strike the specimen in some other place than the one of interest. These effects are undesirable but unavoidable. In addition, flux of bremsstrahlung X-rays produced in the specimen can fluoresce characteristic X-rays from any material that they strike, also giving rise to spurious X-rays.

Single Particle and Ensemble EDS Analysis

The large interaction volume in SEM will most likely lead to backscattered electrons from the substrate wafer, which can give rise to X-rays from parts of the sample that are not intended for analysis. One such example is when point analysis of individual particles is conducted in SEM-EDS. Therefore, one can not be certain that all the measured signal comes from the intended particle, and individual particle analysis is therefore not a trustworthy method using SEM-EDS. Another example is when performing SEM-EDS mapping of some region of the sample. Even if the acquisition time is long, the obtained map will show that there is signal from elements in areas

where they are not present. Electrons can for instance enter the specimen beside a nanoparticle, backscatter so that it ends up in the nanoparticle and generates a characteristic X-rays which is detected and recorded as coming from where the electron entered the specimen, and not from where the X-ray exited. One way to limit the effect is to use long acquisition times. However, one has to consider that the sample might drift and move, in which case long acquisition times can be pointless. The nanoparticles in this project are suspected to show some charging effect due to their rather small contact area with the substrate, so sample drift, especially during point analysis in SEM-EDS, can be expected.

Ensemble measurement of several particles in SEM is more reliable since the signal does not have to be specified from where it originates. For this project, a difficulty of ensemble SEM-EDS measurement is to get enough signal from the nanoparticles so that it can be separated from the noise and subsequently quantified. Since the particles are about 20 nm in diameter, they only constitute a small fraction of the entire interaction volume of the electron beam. To decrease the interaction volume and so increase the fraction of signal coming from the nanoparticles, one can use a lower acceleration voltage or a lower beam current. The main intention of SEM-EDS measurements in this project is to obtain ensemble measurements of the particles. Mapping and point analysis of individual particles will be attempted, however, the signal to noise ratio is suspected to be too low for any reliable quantitative analysis.

EDS analysis of individual nanoparticles in TEM has the advantage of having both a smaller probe and an interaction volume which largely consists of the intended particle. Quantitative analysis of single particles in TEM-EDS is hence considered more reliable then SEM-EDS measurements [2]. To obtain chemical information of more than one particle at a time in a transmission microscope, STEM-EDS mapping is a commonly used method. The small electron probe is then scanned over an area which results in maps which indicate which elements that are present, and from where their signals originate. This method can also be used on a single nanoparticle to investigate whether it contains both Ag and Au, and if the signals are coming evenly from the entire particle, indicating alloying of the elements. In this project, individual particles have been analyzed in both TEM-EDS and STEM-EDS mode. Mapping has been obtained in STEM-EDS mode.

2.4 X-ray Diffraction Spectroscopy

Instead of using electrons to obtain structural and compositional information of spark ablated particles, X-rays can be used [2]. One such X-ray based method is X-ray diffraction (XRD). The technique involves directing X-rays onto a sample which then are elastically scattered by the sample electrons surrounding the atoms. If the sample atoms are arranged symmetrically, the scattered X-rays will interfere constructively (or destructively) with each other in specific angles, determined by Bragg's law shown in equation 18 and in figure 21 below.

$$n\lambda = 2d\sin\theta \tag{18}$$

Here n is an integer, λ the wavelength of the X-rays, d the distance between two diffracting planes and θ the incident angle of the X-ray beam, see figure 21.

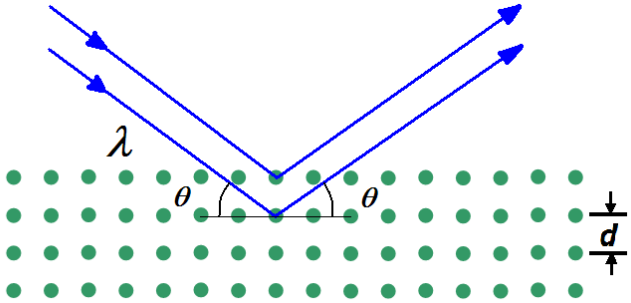

Figure 21: *Incoming X-rays are scattered elastically by a symmetrically arranged specimen. If the X-rays' path length differs by a multiple of their wavelength, they will interfere constructively and produce a reflection spot in the diffraction pattern. Figure developed from [38].*

By measuring the intensity and the angle of the scattered X-rays, information about the symmetry and spacing of the lattice planes in the sample can be acquired. For a large single crystal, similar diffraction patterns that can be seen in a TEM, see section 2.2, can be obtained.

Due to the typical dimension of the X-ray beam (between 1 mm^2 and 1 μm^2), XRD of crystalline nanoparticles involves measuring on many particles at the same time, and is often referred to as *powder* XRD. In this case, one does not obtain the same clear diffraction spots as for single-crystal XRD described above. Instead, all particles, though each one of them have periodically spaced lattices, are randomly oriented on the substrate which means that also the diffraction planes are randomly oriented in reference to the incoming X-ray beam. The same is true for a polycrystalline crystal. Instead of obtaining clear diffraction spots, the pattern consists of intensity rings which are formed by diffraction of the many different orientations of the tiny crystals, see figure 22. From the rings, one can still obtain information about the lattice constant and the distance between diffracting planes. The technique allows for measurements of an ensemble of particles, and the result, therefore, describes the average of the sample, compared to diffraction from a large single crystal [2].

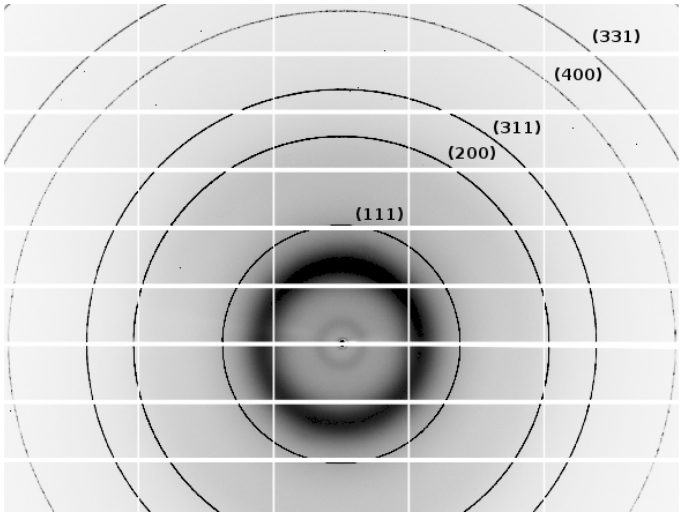

Figure 22: *Powder diffraction pattern of a Si sample. Circles are formed as a result of diffraction from different oriented crystals and planes. The planes have been indexed. Figure taken from [39].*

The intensity distribution from the X-ray diffraction is commonly detected and displayed as a function of two times the angle θ. An example of such a plot can be seen in figure 23. Smaller crystals will lead to broadening of the rings, a phenomenon that can be used to estimate the particle's size. The drawback to broadening of the intensity rings is that the signal to noise ratio decreases, and it can be difficult to obtain sufficient signal for characterization of small nanoparticles. The particles are typically deposited on a substrate which contributes to noise as X-rays can penetrate deeper into a material than electrons [2]. One way to increase the signal from the particles is to use a grazing incidence of the X-ray beam, limiting the path length of the X-rays in the substrate and so the noise. For this project, grazing incidence XRD was used to obtain as much signal from the particles as possible. Since Ag and Au both have the face centered cubic crystal structure and very similar lattice parameters ($a_{Ag} = 4,079$ Å & $a_{Au} = 4,065$ Å) [40], it is likely that the peaks obtained from the XRD measurements of the particles in this project are superimposed. Normally, alloying of materials is indicated by a shift of the peaks in the XRD spectra so that they are positioned closer together. Since the peak shift might not be possible to detect, it might not be possible to determine if the particles consist of an alloy or of pure Ag or Au.

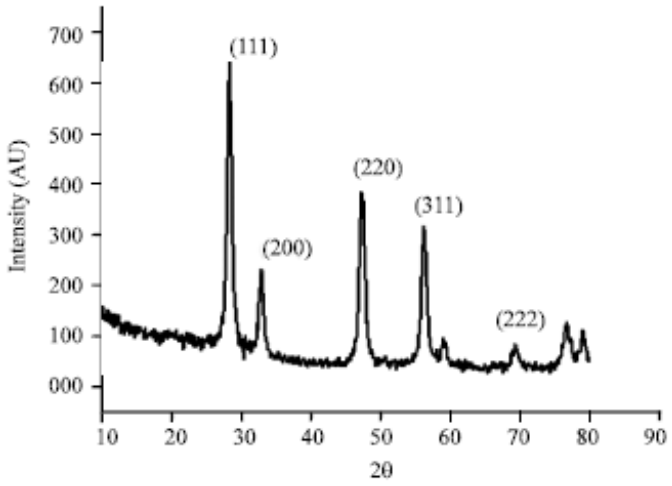

Figure 23: *XRD data from measurements of Ce oxide. The intensity is plotted as a function of* 2θ*. Figure taken from [41].*

3 Methodology

Bimetallic particles of Ag and Au were produced by spark ablation using either alloyed electrodes or one electrode of Au and one of Ag. The general approach used for particle production in this project and the subsequent characterization are described in the sections below, accompanied by illustrative images.

3.1 Particle Production

For this project, different gold and silver alloys (Ag25Au75, Ag50Au50 and Ag75Au25) and pure Ag and Au were used as electrodes, all acquired from Goodfellow. The choice of the material system can be motivated by the fact that both Ag and Au have the face centered cubic crystal structure as well as very similar lattice parameters. The system allows for formation of alloys for all compositions, i.e., they are miscible in bulk, as can be seen in figure 24 below. Other reasons for choosing Au and Ag for the particle production is that neither of the elements are magnetic and they are not expected to oxidize, which allows for easier and more reliant analysis of the particles' morphology and composition. The fact that data acquired already in 2017 was available for analysis also influenced the choice of the present material system.

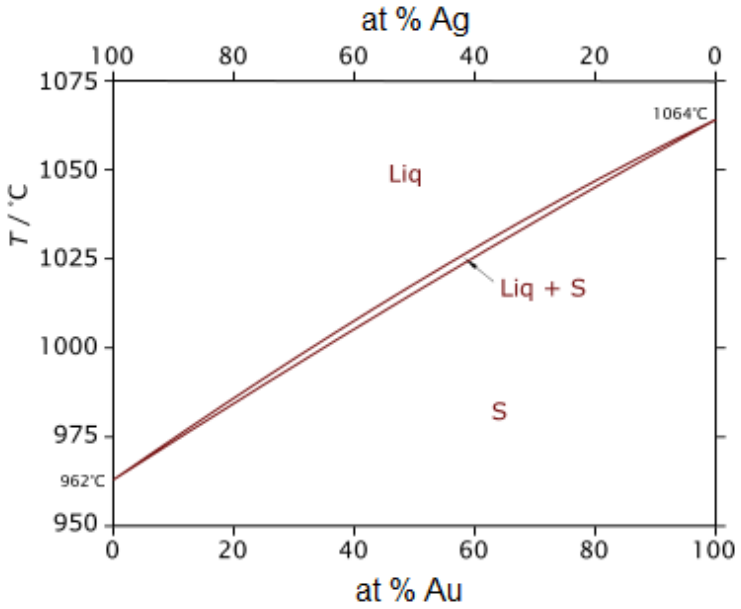

Figure 24: *Phase diagram of Ag and Au, showing full miscibility. Figure developed from [42].*

When the electrode material was decided, the chamber could be assembled. The electrodes were fastened in dedicated electrode holders which can be seen in figure 25 below. One of the electrode holders could be used to control the position of one electrode inside the chamber, thereby allowing for tuning of the electrode gap distance. Other components that were attached to the chamber include a see-through window, a carrier gas inlet, and a carrier gas outlet. O-rings were fastened using clamps between all components and the chamber to minimize gas leakage between the chamber and the outside atmosphere.

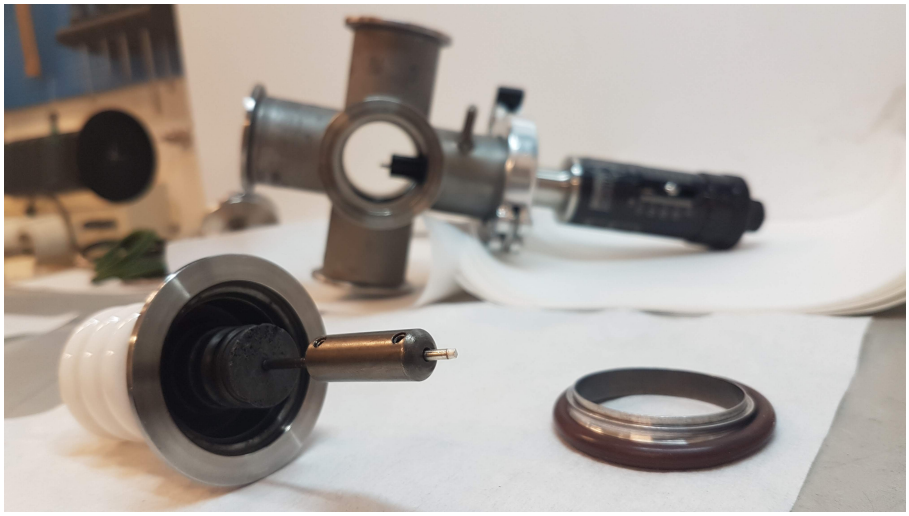

Figure 25: *A picture of the chamber with one electrode holder attached. The electrode is just visible inside the chamber. The other electrode and its holder is shown to the left and the O-ring used when attaching the electrode holder to the chamber is visible to the right.*

When all parts were attached to the chamber, it was ready to be inserted to the SDG system. This means that it was connected to the carrier gas flow, one of the electrodes was connected to the high voltage source (hence the protective box surrounding the left electrode) and the chamber itself was grounded using thick copper wires, see figure 26 below. The wires were there as a safety precaution if the spark were to hit the inside of the chamber instead of hitting the opposing electrode. The figure shows the SDG system in action, and the plasma is visible through the chamber window, and in the inset to the right.

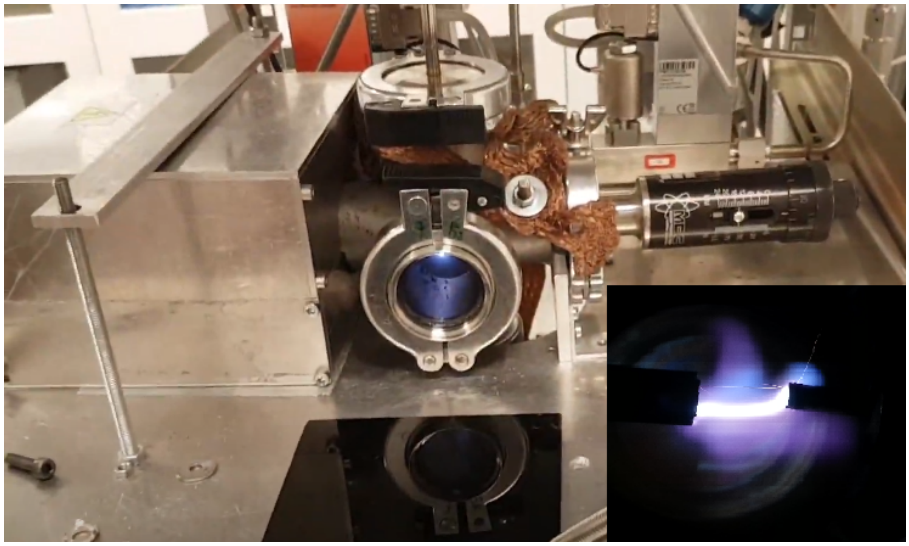

Figure 26: *The chamber attached to the SDG system and in action. The left electrode holder which is connected to the high voltage source is protected by a metal box. Grounded copper wires are attached to the chamber. Inset: Image of a plasma channel between two electrodes, courtesy of the engineered nanoparticle group at NanoLund.*

The SDG system setup used is shown in figure 27 (and figure 4 in the SDG theory section). DMA1 was bypassed in order to achieve a higher particle concentration and so reduce the time needed

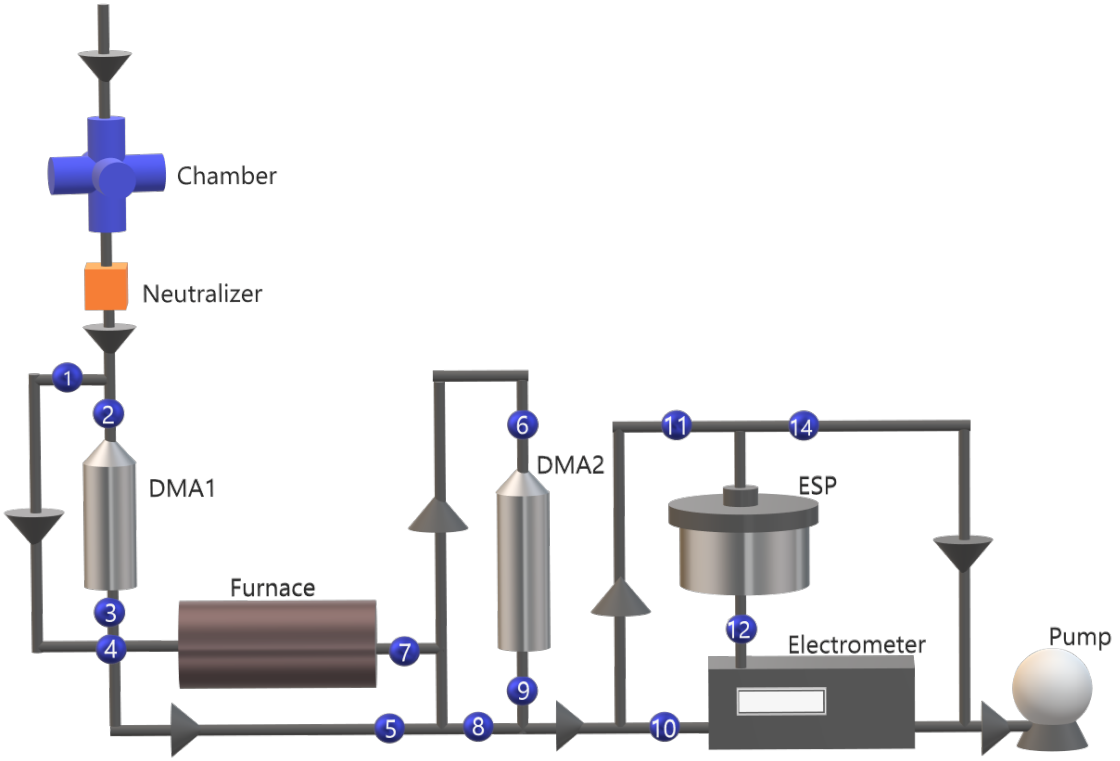

Figure 27: *The SDG system setup used in this project. The first DMA is always bypassed and the ESP is bypassed when particle deposition is not desired.*

for deposition. When not depositing particles, e.g., when tuning the production parameters and conducting online measurements of the particles, the ESP was bypassed. During deposition, all particles entering the ESP, end up in the ESP, and so the particle concentration is not known during deposition using this setup. The neutralizer was a Ni^{63} bipolar diffusion charger, the furnace a Lenton LTF tube furnace and DMA2 a Vienna-type DMA. The ESP used was custom built and the electrometer was a TSI Electrometer Model 3068B. Nitrogen was used as a carrier gas, the flow rate was set to 1.68 liters per minute, and the system pressure was held at 1015 mbar, which is commonly used for the setup. Typical parameter values for production of spark ablated Ag-Au particles are shown in table 1. Some parts of the system are controlled by a computer using a LabView program. The software can control the driver voltage and current, the DMA settings, the pressure and the carrier gas flow rate. Other parameters such as the electrode gap distance, the furnace temperature and the deposition are controlled manually on the different parts of the SDG setup.

SDG parameter (unit)	Furnace temp. (℃)	Electrode gap dist. (mm)	Driver voltage (kV)	Discharge voltage (kV)	Driver current (mA)	Energy per spark (mJ)
Value	700	1-2,5	12	2-3,4	10-18	74

Table 1: *Some values of the SDG parameters used for nanoparticle production in this project.*

Before deposition, the size distribution of the particles was obtained using DMA2. A typical result is shown in figure 28 below.

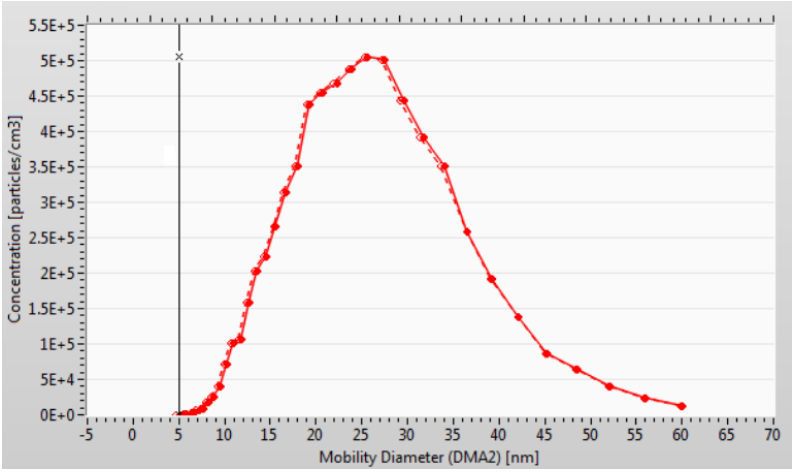

Figure 28: *Offline characterization of the produced particles using DMA2. The plot shows the particle concentration as a function of their mobility diameter (related to the particles' diameter and charge).*

3.1.1 Deposition

When a diameter was specified and the corresponding particle concentration known, an algorithm developed in [32] was used to calculate the time needed for deposition of a certain coverage of particles on the substrate. For analysis in TEM and SEM a coverage of about 40-80 particles $/\mu m^2$ was obtained. The deposition time varied between a few seconds to several minutes. Deposition intended for XRD measurements needed much higher coverage (several thousands particles$/\mu m^2$) on the substrate to ensure that a signal can be acquired, see figure 29. The time needed for the XRD deposition was about 5 hours.

The substrates for particle deposition and characterization are the same for SEM and XRD, namely silicon wafers with an inherent amorphous silicon oxide on the surface. For TEM analysis, a carbon coated Cu grid was used. Since the grid is small and difficult to handle with typical tweezers, it was attached to a silicon wafer using silver glue, see figure 29. The deposition procedure was thereafter the same as for SEM and XRD. After deposition, the samples were stored in ambient pressure in small sample boxes. When it was time for TEM analysis the Cu-grid was detached from the silicon wafer and subsequently analyzed.

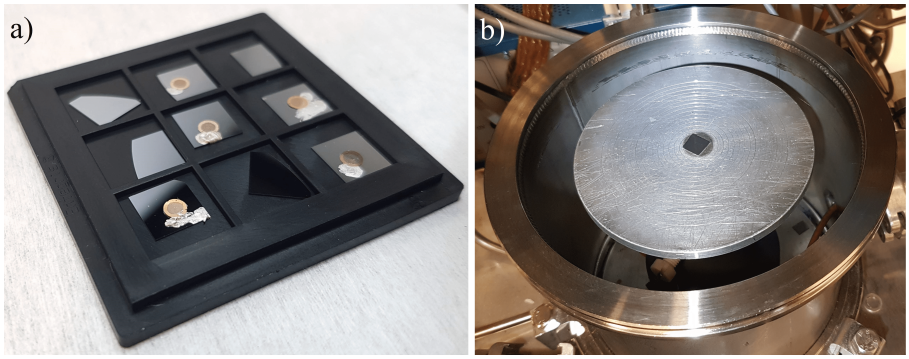

Figure 29: *a) Samples of particles deposited on silicon wafers. Some wafers have Cu-grids attached using silver glue to enable TEM-analysis of the particles. b) Spark ablated particles deposited on, (and around) a silicon wafer. The high coverage (visible with the naked eye!) is intended for XRD analysis.*

Since different electrode materials are used, and some particles get stuck in the chamber instead of leaving with the carrier gas flow, see figure 30, the chamber is cleaned when a new pair of electrodes should be used. Cleaning was performed in a fume hood, using personal protection, and involved wiping the interior of the chamber with a clean room cloth drenched in a solvent, such as ethanol or isopropyl alcohol.

Figure 30: *Some particles are not transported away from the chamber with the carrier gas and might get stuck on the electrode or the electrode holder.*

3.2 Offline Characterization

3.2.1 SEM & SEM-EDS

After a first attempt to view and analyze the deposited particles in a GeminiSEM 500 from Zeiss (capable of EDS), it was clear that the initial coverage (40 particles/μm^2) was too low for obtaining signal from ensemble SEM-EDS measurements of the particles. Therefore, a second round of depositions on the same samples were made. With a higher particle coverage (70-80 particles/μm^2), characterization of the particles could, to some extent, be carried out using a JEOL 30kV FSEM. Only one sample of 30 nm produced nanoparticles was analyzed, see the Si wafer attached to an aluminium stub in figure 31. Both point spectra and maps of larger areas were obtained. The alloy electrodes were either screwed tight to or glued by conductive carbon tape onto brass stubs and analyzed with EDS in the JEOL FSEM, see figure 31. Electron images of both the nanoparticles and the electrodes were acquired using a SE detector. The composition of the electrodes were analyzed to see if the measured compositions agree with the specified composition from the electrode producing company. The analysis done in this project is, however, thought to be less reliable than the composition specified by the company.

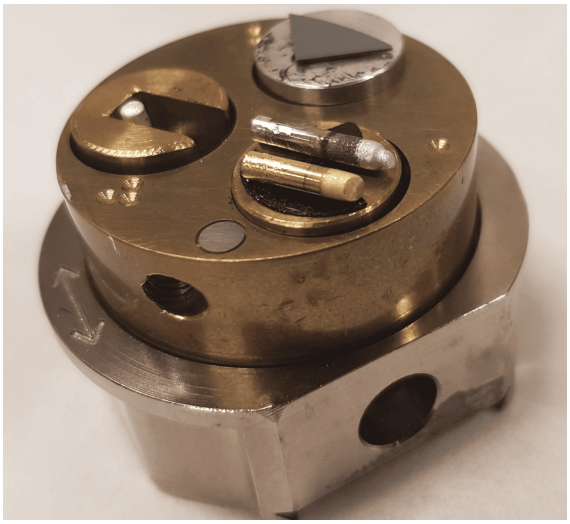

Figure 31: *A sample with 30 nm particles deposited on a Si wafer attached to an aluminium stub by conductive carbon tape. Alloyed electrodes are either screwed tight or attached by carbon tape to brass stubs. The stubs are fastened to a sample holder which can be inserted in the microscope.*

The AZtec software helped identify characteristic peaks in the spectras and deconvolute elements besides those of interest for the final quantification, e.g., Ag and Au. Some common deconvolution elements were Si, C, O, Zn, Cu and Al.

3.2.2 TEM, STEM, TEM-EDS & STEM-EDS

TEM images of different magnifications were acquired of the particles using a JEOL 3000F TEM and a Hitachi 300 kV Environmental Transmission Microscope at the national Center for High Resolution Electron Microscopy in Lund. Both microscopes offer EDS analysis, and quantitative measurements of individual particles were obtained with EDS in TEM mode. 15-16 particles produced by Ag-Au alloy electrodes, and 30 particles produced by one Ag and one Au electrode, were analyzed and quantified. The data from 2017 contained 9-19 quantified particles produced by Ag-Au alloy electrodes. All particles had a diameter of about 20 nm and had been generated using similar spark ablation production parameters. STEM-EDS measurements were only obtained of particles produced by two different electrodes in one configuration: Ag as the anode and Au as the cathode. Maps of a few particles were obtained.

The AZtec software helped identify characteristic peaks in both the TEM-EDS and STEM-EDS spectras and deconvolute elements besides Ag and Au. Some common deconvolution elements were Cu, C, O, and Si. For the data from 2017, the deconvolution elements also included Fe and Al. For the quantification procedure, the density and thickness of the sample was manually specified in the software. The density was calculated using the electrode composition used for production and the thickness was set to the particles diameter, 20 nm. The program used the specified numbers for the density and thickness as a basis for its calculations and iterated a new density from the intensity measurements. This is done until the density and thickness matches the obtained spectral data.

3.2.3 Statistical Analysis of the Nanoparticles' Composition

To analyze and compare the acquired compositions of the nanoparticles, statistical analysis of the data was performed. Estimators of the population mean $\overline{X}$, variance s^2 and standard deviation s were calculated using the formulas 19, 20, and 21 shown below. It was here assumed that a random sample was drawn from a normal distributed population with mean μ and variance σ^2. To enable this analysis, the individual samples (the particle compositions) X_i, $i = 1, ..., n$ are also assumed to be independent of each other.

$$\overline{X} = \frac{1}{n}\left(\sum_{i=1}^{n} X_i\right) \tag{19}$$

$$s^2 = \frac{1}{n-1}\sum_{i=1}^{n}(X_i - \overline{X})^2 \tag{20}$$

$$s = \sqrt{\frac{1}{n - 1.5 + \frac{1}{8(n-1)}}\sum_{i=1}^{n}(X_i - \overline{X})^2} \tag{21}$$

Here $\overline{X}$ is the sample mean, s^2 the unbiased sample variance, and s the unbiased sample standard deviation [43]. n is the size of the sample, e.g., the number of individually quantified nanoparticles. The reason for using an unbiased sample standard deviation, is that by taking the square root of the unbiased sample variance, a bias is introduced by the square root function. One way to better estimate the sample standard deviation is to use the corrected expression shown in 21. Note that s in equation 21 is not equal to the square root of s^2 in equation 20. To compare the quality of the variance estimates for the measured samples, the mean error of the variance can be calculated as shown in equation 22 below.

$$d(s^2) = s^2\sqrt{\frac{2}{n-1}} \tag{22}$$

To compare the confidence of the estimates of the different population means, a confidence interval for μ, when σ is unknown, with a confidence of $1 - \alpha$ [44] is calculated for each sample:

$$I_\mu = (\overline{x} \pm t_{\alpha/2}(n-1) \cdot d(\overline{X})) \tag{23}$$

Here the quantiles $t_{\alpha n}$ for different values of α and n are taken from a table of the t-distribution, and $\overline{x}$ is the measured sample mean. Confidence intervals with 95% confidence ($\alpha = 0.05$) will be calculated. $d(\overline{X})$ is the standard error of the mean (also SE of mean) and is calculated using formula 24. SE depends on the sample size n and can give an indication of the quality of the mean estimation from the sample [44]. The statistical analysis was performed in Excel and Matlab.

$$SE = d(\overline{X}) = \frac{s}{\sqrt{n}} \tag{24}$$

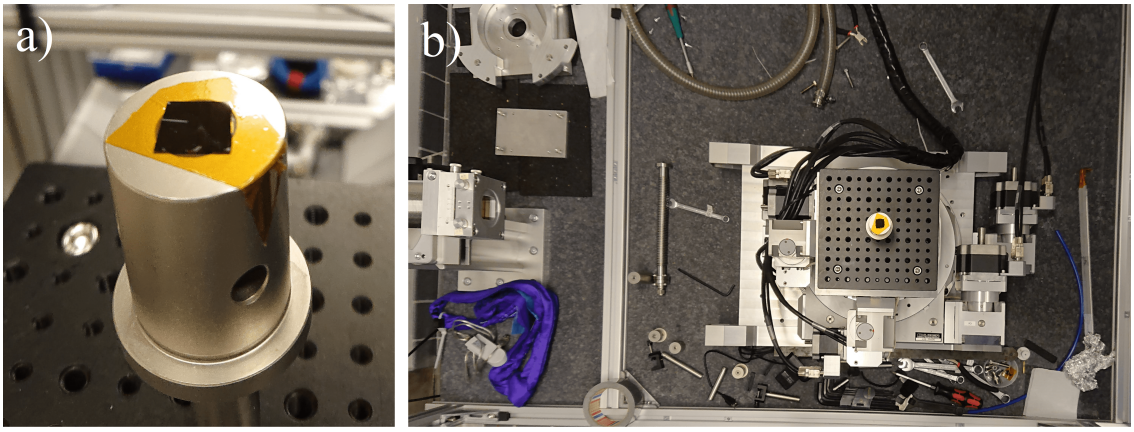

Figure 32: *a) A closeup on the sample wafer attached to the sample holder. b) The XRD setup from above. One detector can be seen to the left in the image. The sample holder's position can be controlled very precisely from a remote computer.*

3.2.4 XRD

The XRD measurement was conducted in reflection mode at a setup available in the department of Synchrotron Radiation at Solid State Physics in Lund. The sample was attached to a sample holder whose position could be controlled by a computer, see figure 32. A Molybdenum 17,5 keV laser with a wavelength of 0,17 Å hit the sample at a grazing incidence and the diffracted X-rays were detected by two detectors from Dectris, model PILATUS3 X 300K CdTe. The measurements were done remotely, and everything could be controlled by a computer. First, the sample was aligned in x, y, and z direction so that about half the laser intensity was detected. Second, the sample was tilted so that a grazing incidence (about 0,2 degrees) of the laser was obtained. The third step included choosing an area of interest of the diffraction pattern, and this was decided in agreement with previous XRD measurements of similar samples. Finally, the measurement procedure could be specified. The sample was turned 90 degrees in 180 steps, and one image was recorded in each step. The measurement took about 8 hours and was performed overnight.

For analysis of the obtained intensity images, ImageJ was used to subtract noise and subsequently integrate the intensity from all images. The result was a black and white intensity image of the diffracted X-rays from the sample. Using Matlab, a short script was then used to plot the integrated intensity as a function of 2 times the angle θ. The plot was then compared to reference plots of pure Ag and Au powder diffraction patterns taken from [45] and viewed in Mercury.

4 Results & Analysis

During online characterization of the particles, it was observed that some combinations of production parameters lead to higher or lower particle concentrations. For example, it was more difficult to generate high particle concentrations using electrodes containing a lot of Ag, such as Ag75Au25. Combining this with a high energy-per-spark resulted in practically no particles that were larger than 30 nm, with most particles having a mobility diameter of 15 nm, see figure 33 below. From cleaning away waste material from the chamber, it was further confirmed that electrodes containing a high Au percentage ablate more strongly than those containing a high percentage of Ag. This has been found to be in line with the ablatability ratio with Au of the elements, i.e., how easily an element is ablated compared to Au. The ablatability of Au is set to 1, and then Ag has an ablatability ratio of 0.73 [2].

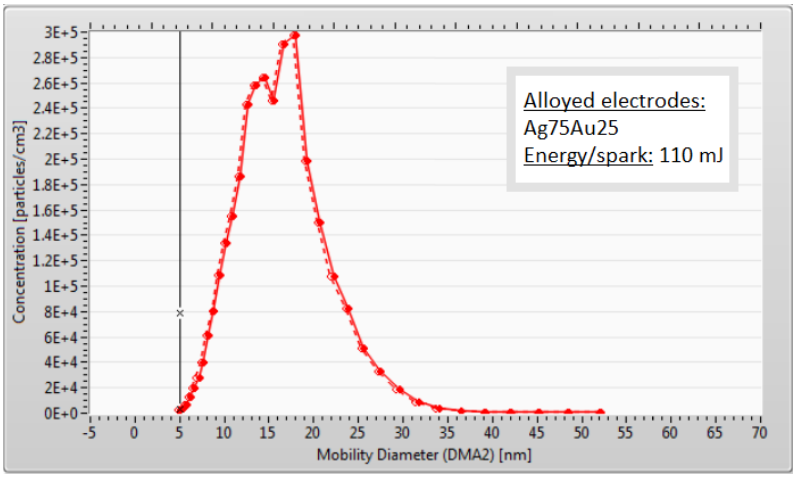

Figure 33: *Example of a particle concentration distribution when using electrodes with high Ag content (Ag75Au25) combined with a high energy-per-spark.*

In the following sections, results from offline characterization of the spark ablated nanoparticles are presented. First, the morphology of the particles acquired in SEM and TEM is shown and briefly commented, together with some SEM-images of the alloyed electrodes. Thereafter, the compositional results of the nanoparticles will be presented with focus on individual particles' composition. The procedure of some basic statistical analysis of the TEM-EDS data from both 2017 and 2021 is presented. Finally, results from SEM-EDS and XRD ensemble measurements of the particles are presented. The available results of the particles produced in 2017 are TEM-images and TEM-EDS data. Results from SEM, SEM-EDS and XRD are only available of particles produced in 2021.

4.1 Morphology

4.1.1 SEM Images

Figure 34 shows SE-images of spark ablated nanoparticles, produced using alloyed Ag25Au75 electrodes in 2021, at different magnifications acquired in a SEM. The images appear a bit unclear due to drifting of the sample during acquisition. Presence of some larger splashed particles could be seen, and proved to be particularly useful for obtaining focus on the smaller particles. The nanoparticles appear to be evenly distributed on the sample surface with about the same surface concentration as intended (40-80 particles/μm^2) during production and deposition.

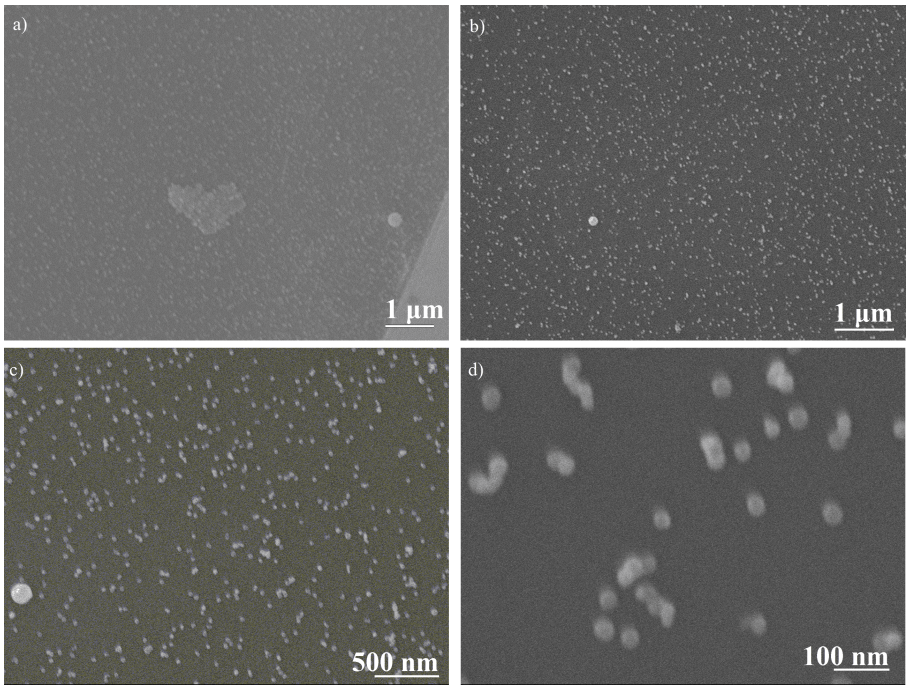

Figure 34: *SEM SE images of nanoparticles produced in 2021 using Ag25Au75 alloyed electrodes. Some larger splashed particles can be seen in a), b) and c) but not in d). The images look unsharp due to extensive sample drift.*

SE-images of two electrodes and their surfaces can be seen in figure 35. The surface appears lava-like, probably as a result from the heating of the electrode caused by the plasma and sparks during particle production. Similar results of the surface of the electrodes have previously been reported and are closely studied in [46].

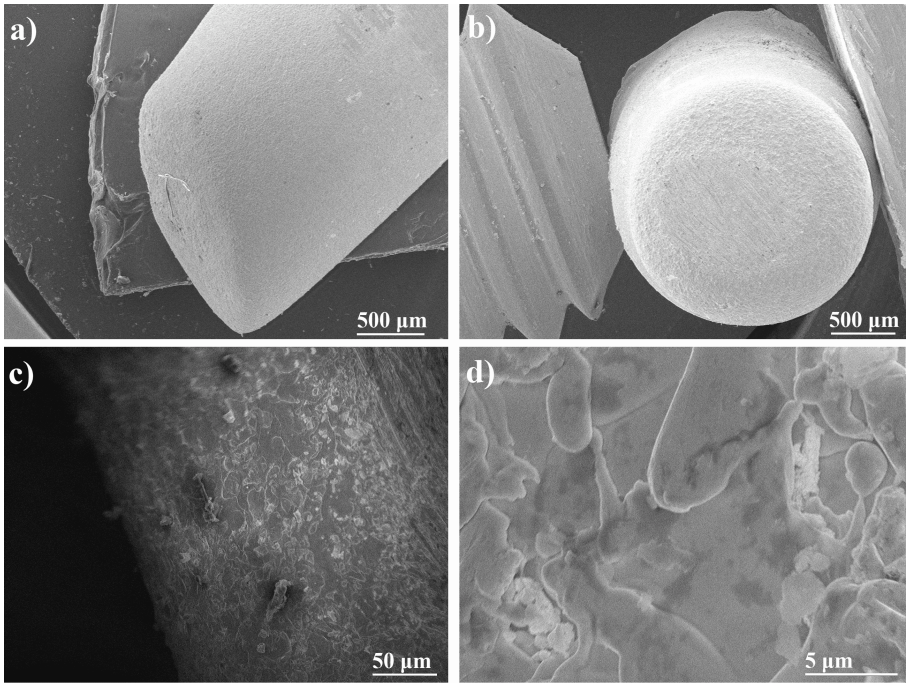

Figure 35: *SEM images of alloyed electrodes. a) An electrode in profile on a conducting carbon tape. b) A screw holds the electrode in place allowing for imaging of the ablated surface. c) and d): Close-up images of the surface of the electrodes.*

4.1.2 TEM Images

Figure 36 shows TEM images of nanoparticles generated in 2021 using Au as the anode and Ag as the cathode, while the nanoparticles in figure 37 are generated in the opposite configuration. From the c) and d) images in both figures, it seems as if the particles are close to spherical and crystalline, indicating a high enough temperature of the sintering furnace.

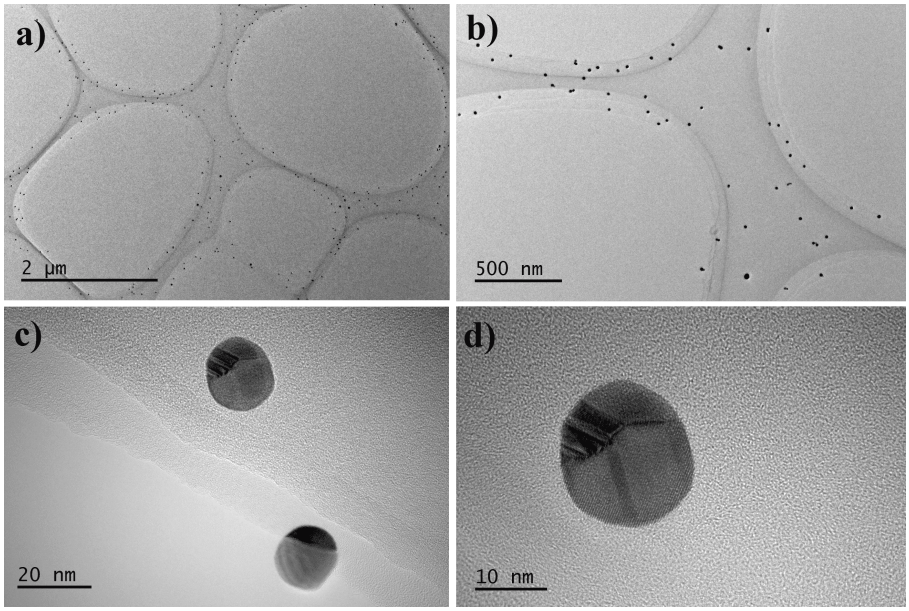

Figure 36: *TEM images of nanoparticles generated in 2021 with Au as anode and Ag as cathode. a) Particles deposited on a lacey carbon grid, and a close-up is shown in b). Images of magnified particles in c) and d) reveal crystallinity of the nanoparticles.*

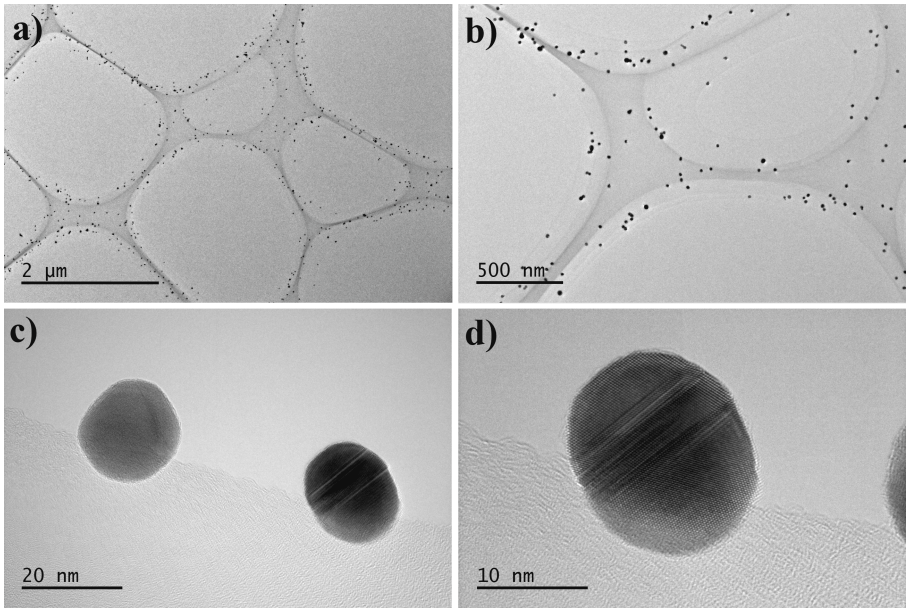

Figure 37: *TEM images of nanoparticles generated in 2021 with Ag as anode and Au as cathode. a) and b) show particles deposited on a lacey carbon grid. The nanoparticles in c) and d) display faceted surfaces.*

In figure 38 TEM images of single nanoparticles produced in 2021 and 2017 are shown. Note that the scale bars are of different sizes in the images. The nanoparticles in a) and d) are generated with electrodes with composition Ag25Au75. The nanoparticles in b) and e) are generated from Ag50Au50 electrodes and the nanoparticles in c) and f) are generated with the Ag75Au25 alloyed electrodes. All particles are spherical and crystalline, and indications of twin boundaries exist.

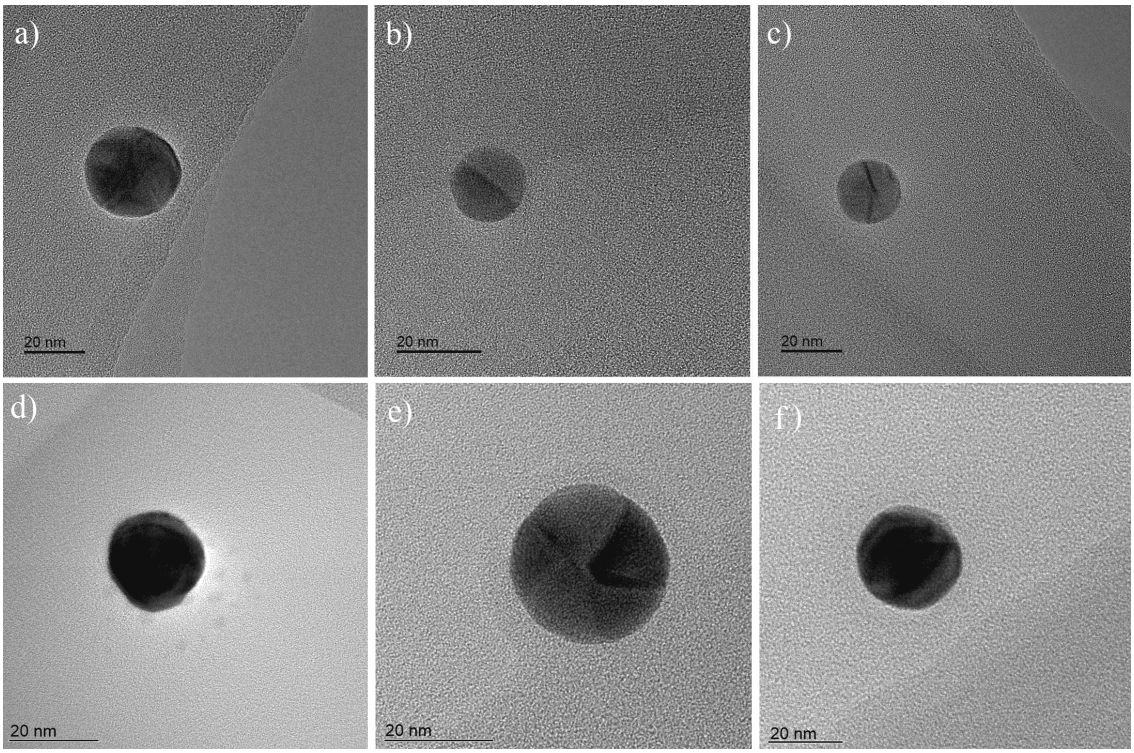

Figure 38: *TEM images of nanoparticles generated in 2021 (a-c) and in 2017 (d-f) with alloyed electrodes. a) and d) Ag25Au75. b) and e) Ag50Au50. c) and f) Ag75Au25.*

The TEM images in figure 38 show that the nanoparticles produced in 2017 and 2021 are very similar. Both appear crystalline, have similar diameters and are next to spherical, indicating that a high enough sintering temperature for compaction of the agglomerates were used, which was expected from the literature [31]. The good reproducibility of the nanoparticles at different times indicates a high stability of the SGD system used in this project.

4.2 Composition

TEM-EDS spectras of individual particles were collected during about one minute. No apparent EDS system artifacts such as escape peaks or sum peaks were observed. Some illumination system artifacts such as characteristic peaks originating from elements in the microscope, Cu, Al and Fe for example, were observed.

k-factors and Absorption Correction

The k-factors for Ag and Au were approximately the same ($k_{Ag} \approx 1,7$ and $k_{Au} \approx 2,5$) for both the TEM-EDS data from 2017 and the one acquired in 2021. The absorption correction was found to be around unity for both Ag and Au in all TEM-EDS measurements. The k-factor was calculated

by the AZtec software using the theoretical approach described in section 2.3.

For the SEM-EDS measurements, it was difficult to obtain enough signal for quantification of the nanoparticles, and the k-ratios (the ratio between the k-factor of the sample element and its factory standard) differed a lot between measurements. Quantitative data with SEM-EDS was only obtained of the alloyed electrodes, not the nanoparticles. Mapping of the particles could, however, indicate presence of Ag and Au.

4.2.1 Individual Particle Composition

STEM-EDS-mapping of individual particles from 2017 and 2021 are presented in figure 39 and 40, respectively. Signals from Ag and Au are clearly visible and evenly distributed inside the particles, indicating alloying of the elements which is expected from the phase diagram and literature. Quantitative analysis using STEM-EDS of one particle produced in 2021 using Ag as the anode and Au as the cathode showed an Ag content of 22,3 atomic percent, which agrees with the TEM-EDS results, presented in figure 44 below, from the same sample.

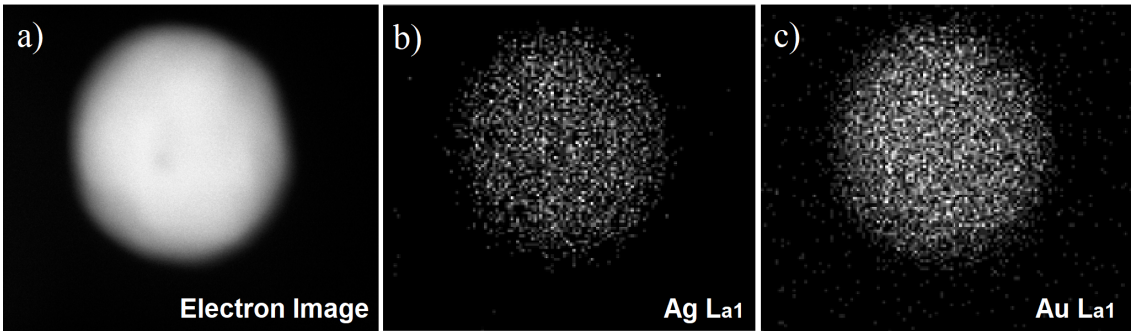

Figure 39: *STEM-EDS mapping of a single particle generated in 2017 with alloyed (Ag50Au50) electrodes. a) STEM image of a nanoparticle. STEM-EDS signal from b) Ag and c) Au. The particle is 29 nm in diameter.*

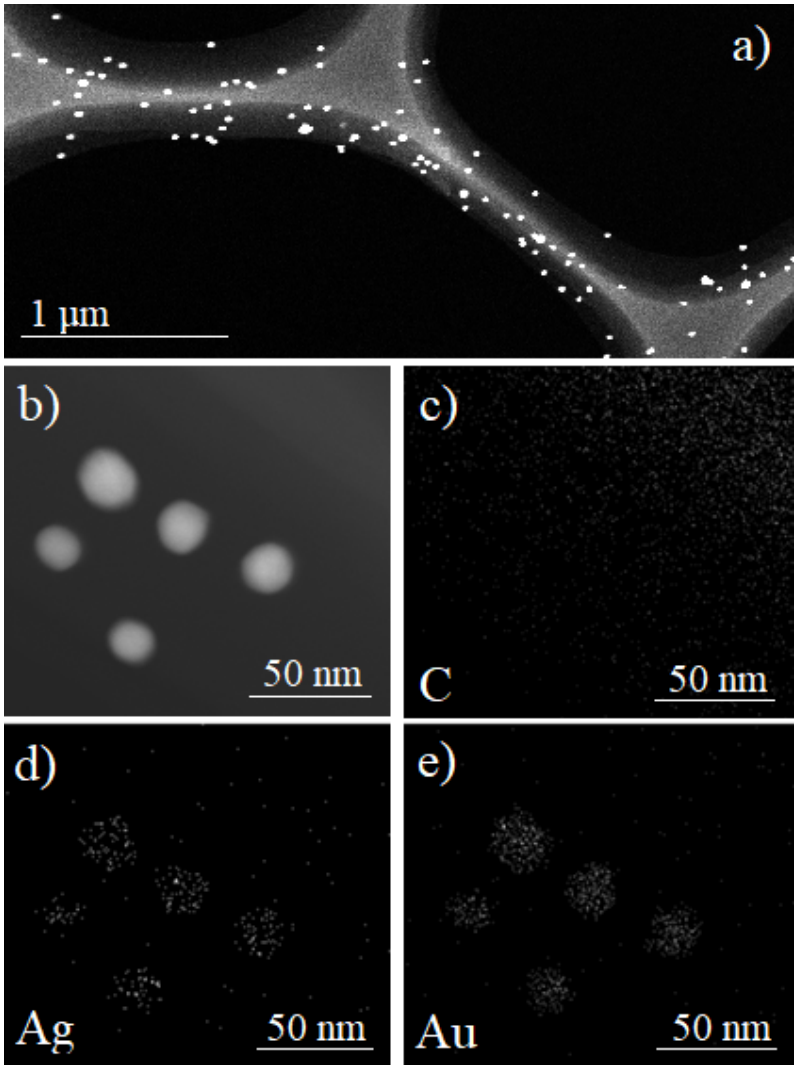

Figure 40: *a) STEM image of nanoparticles from 2021, the carbon from the lacey carbon film is also visible. b) STEM image of 5 nanoparticles that are mapped by STEM-EDS showing c) signals from C, d) Ag, and e) Au. The Ag and Au signals seem to originate from the particles.*

In figure 41 an example of an TEM-EDS spectra of a single particles is shown. Signals from both Ag and Au can be seen, as well as signals from C, O and Cu.

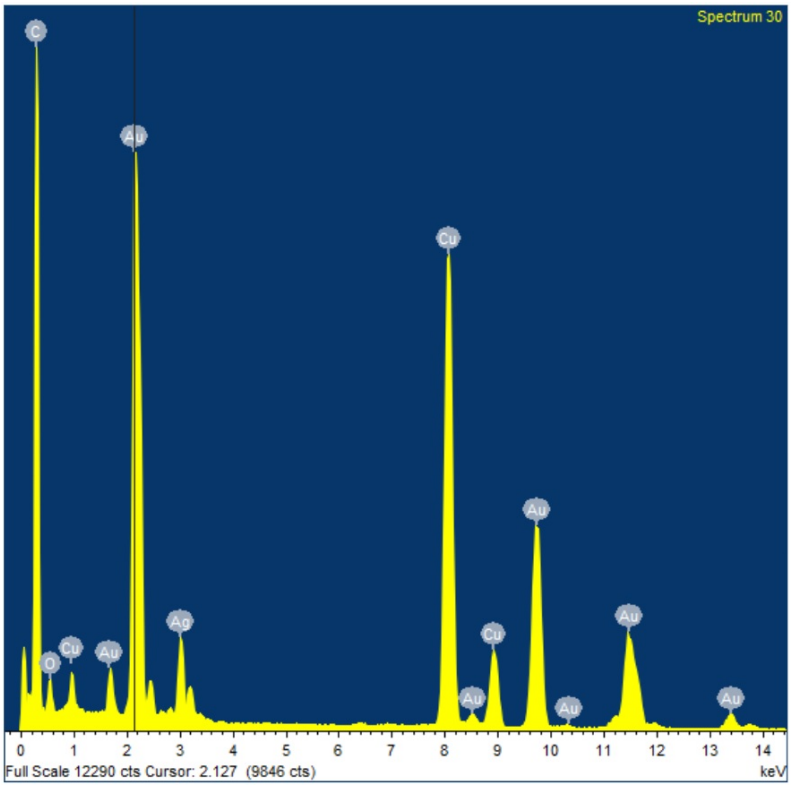

Figure 41: *A TEM-EDS spectra of an individual particle produced using two different electrodes. Here Ag was the anode and Au the cathode.*

Individual particle composition was acquired from TEM-EDS and histograms of the results are presented in figure 42, 43 and 44. The figures show the number of measured particles with a certain Ag atomic composition, and the average and unbiased standard deviation are shown in the figure legends. Figure 42 shows data from 2017 of particles generated using alloyed electrodes. Data from 2021 where particles were produced with alloyed electrodes is shown in figure 43, and figure 44 presents data from particles generated with one electrode of Ag and one of Au. From the general shape of the histograms, indicating normal distributions, the assumption made in section 3.2.3 that the samples are taken from a normal distributed population can, to some degree, be motivated. The raw data of the individual compositions of the particles from both 2017 and 2021 used for analysis in this project are available upon request, preferably by email to the author.

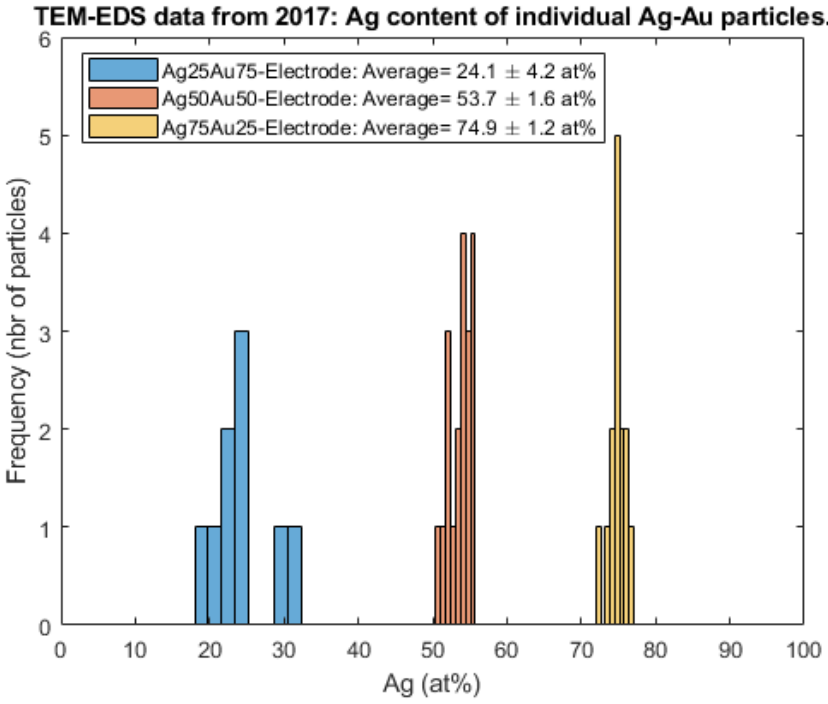

Figure 42: *Analyzed TEM-EDS data from 2017. Histograms showing the number of measured particles with a certain Ag atomic content. The average and the standard deviation of the measured particles' Ag content in at% are shown in the legend.*

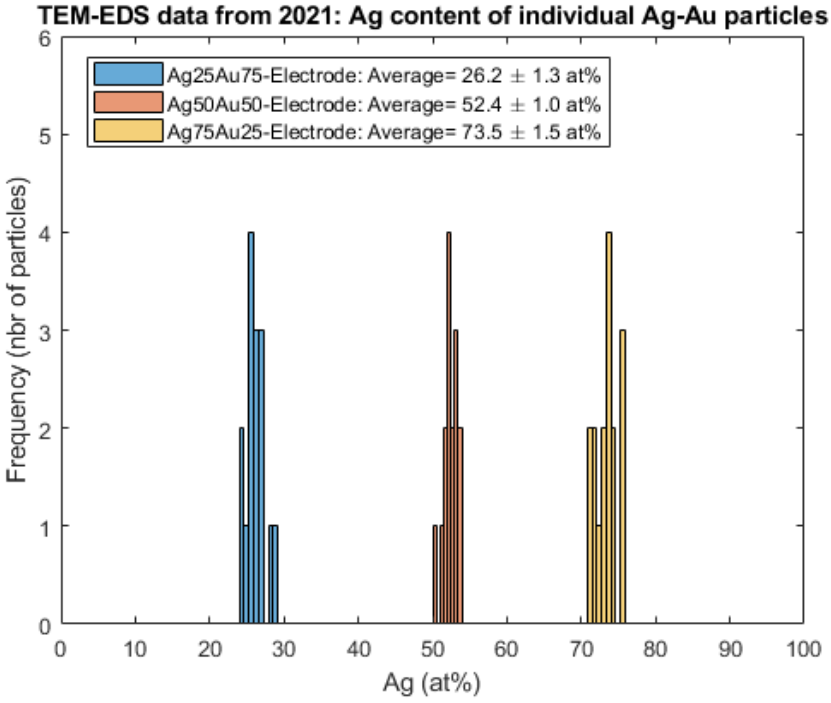

Figure 43: *Analyzed TEM-EDS data from 2021. Histograms showing the number of measured particles with a certain Ag content. The average and the standard deviation of the measured particles' Ag content in at% are shown in the legend.*

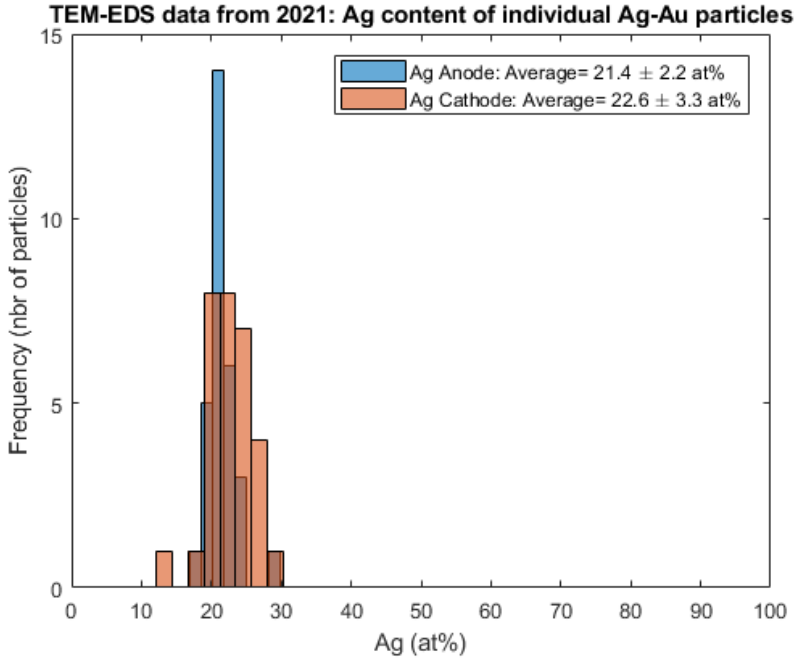

Figure 44: *Analyzed TEM-EDS data from 2021 of nanoparticles produced with one Ag and one Au electrode. The histograms show the number of measured particles with a certain Ag atomic content. The average ± the standard deviation of the measured particles' Ag content in at% are shown in the legend.*

The variance for each sample is plotted against its average atomic percent Ag particle content

in figure 45. Error bars represent the mean error of the variance and indicate how good of an estimate the sample variance is for the population variance. Data from both 2017 and 2021 is represented.

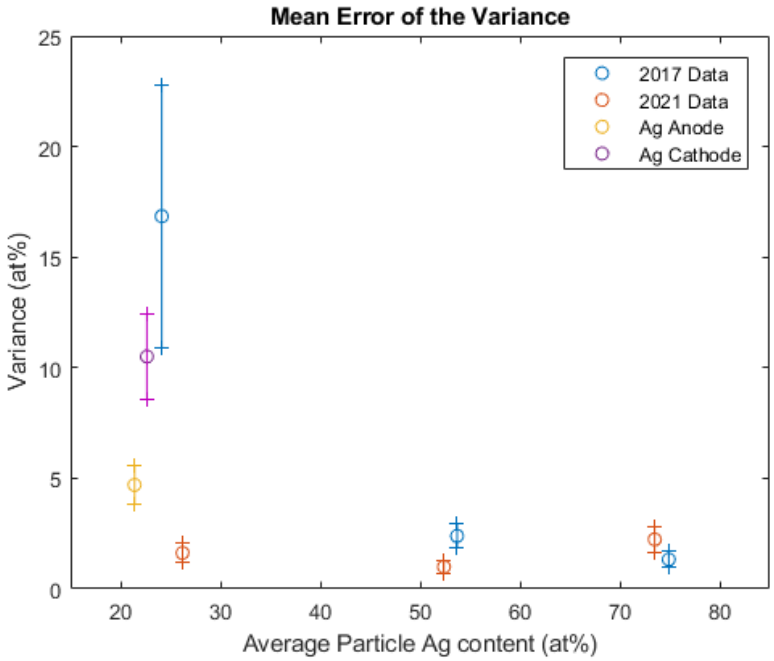

Figure 45: *The variance (circles) of the measured samples with different average particle compositions. The error bars are the mean error of the variance.*

The figure shows that most samples have a variance below 3 atomic percent, except for the sample produced 2017 with the Ag25Au75 electrodes and the samples produced with one Ag and one Au electrode in 2021. The large variance (about 16 atomic percent) of the 2017 data from the Ag25Au75 electrodes is thought to mainly be due to a small sampling size of only 9 quantified particles. Though the sampling size was large (n=30) for the particles produced with two different electrodes, the variance (about 5 and 10 atomic percent) and the mean error of the variance is larger than for all but one of the samples produced with alloyed electrodes, both in 2017 and in 2021.

In figure 46, the calculated 95 percent confidence intervals of the corresponding population mean are shown. The mean is here set to zero to give a more clear overview of the size difference of the confidence intervals. The samples and the sample size of the corresponding intervals are shown in textboxes in the figure.

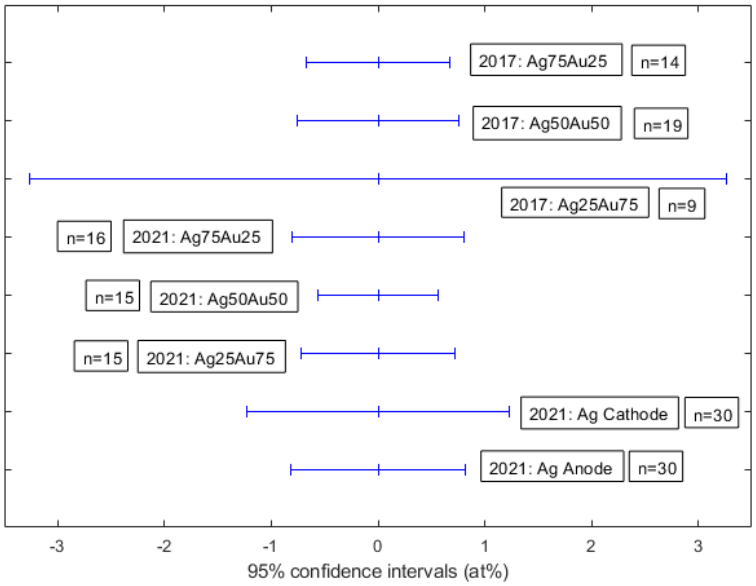

Figure 46: *Confidence intervals with 95% confidence that the real sample mean lies within the interval. Note that the mean here is set to 0 to compare the interval sizes. The number of measurements, n, for each sample is given in the figure.*

Most intervals in figure 46 show a high confidence that the population mean lies within or just above ± 1 atomic percent of the estimated sample mean. One interval (Ag25Au75 from 2017) stands out from the crowd showing an interval of just above 3 atomic percent around the sample mean. This sample has a significantly lower sample size (n=9) compared to the other sample sizes (n=14-30).

Table 2 shows the difference between the electrode Ag atomic composition and the average particle composition obtained with TEM-EDS. The blue columns indicate data from 2017. The difference in the composition of samples produced using alloyed electrodes is quite low, the largest being -3,7 atomic percent. Using two different electrodes for production of the particles, the difference is high, almost 30 atomic percent, and is thought to originate from the different ablatabilities of the materials, where Au is known to ablate more easily than Ag. Using Ag as the cathode, more Ag is ablated compared to when it is used in the anode position. This is in line with the theory that the negative cathode is ablated more strongly due to the attraction of heavier positive ions compared to the lighter negative electrons striking the anode during the spark.

Table 2: *Ag composition of electrodes and the average Ag particle composition obtained by TEM-EDS for all samples. The difference is shown in the rightmost column. The first 3 rows of the table contains results from nanoparticles acquired in 2017, indicated by an asterisk (*).*

Sample	Electrode (Ag at%)	TEM-EDS (Ag at%)	Difference (at%)
Ag25Au75*	25	24,1	0,9
Ag50Au50*	50	53,7	-3,7
Ag75Au25*	75	74,9	0,1
Ag25Au75	25	26,2	-1,2
Ag50Au50	50	52,4	-2,4
Ag75Au25	75	73,5	1,5
Ag anode	50	21,4	28,6
Ag cathode	50	22,6	27,4

4.2.2 Ensemble Composition

Below, SEM-EDS results from both the nanoparticles and the electrodes are presented. The results from the XRD measurements are shown last in this section.

SEM-EDS

It was difficult to obtain enough Ag and Au signals from the nanoparticles with SEM-EDS. No apparent EDS system artifacts such as escape or sum peaks were observed. Some illumination system artifacts such as characteristic peaks from elements in the microscope, Al for example, were observed.

Figure 47 shows a SEM SE image of a sample wafer and an indication of where a point measurement with SEM-EDS is acquired, and the corresponding spectrum. The elements identified are Si, C and Al, and no signal from Ag or Au is detected at this low magnification.

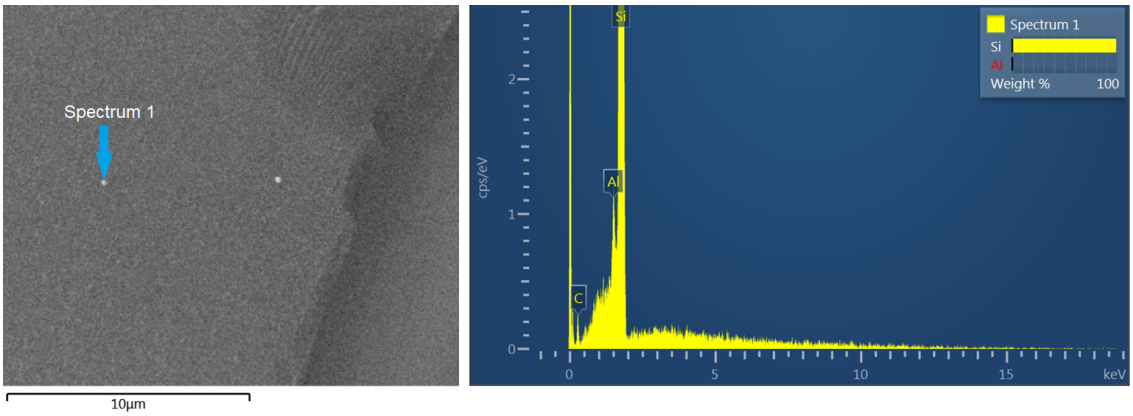

Figure 47: *Left: Electron image of a sample, produced using alloyed Ag25Au75 electrodes, in low magnification. A point spectra on a large splashed particle was acquired and is shown to the right. Neither Ag nor Au is detected.*

Figure 48 shows a SEM-EDS mapping of a larger splashed particle surrounded by many smaller nanoparticles. Signal from both Ag and Au is obtained as can be seen from the sum spectrum and from the origin of the signals. The splashed particle seems to consist of Ag and Au together with some traces of carbon. There seems to come a small Ag and Au signal from the nanoparticles in the map, however, it is not concentrated enough to be determined to come from individual particles.

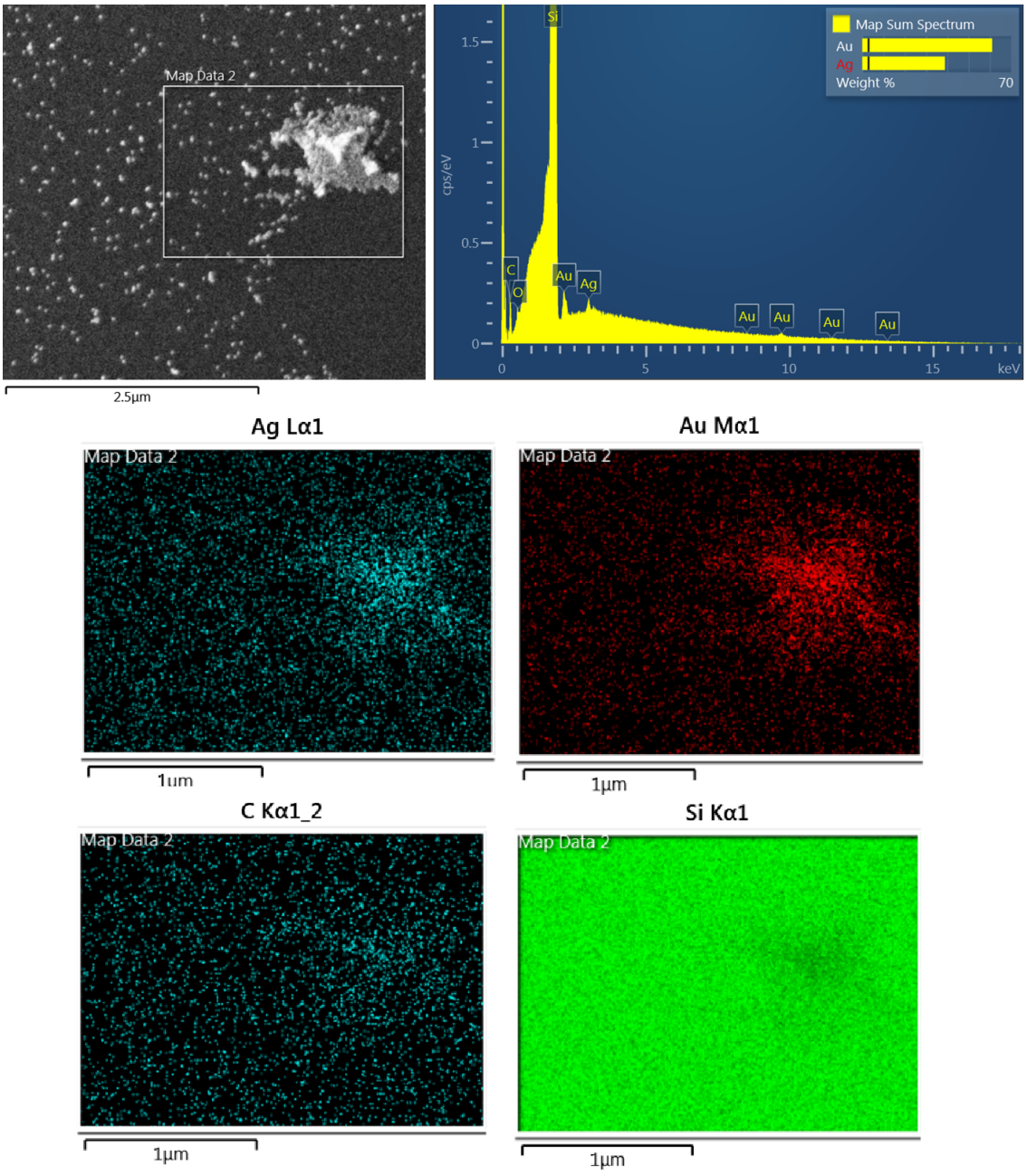

Figure 48: *SEM-EDS mapping of a large splashed particle and some smaller nanoparticles. Besides Si, the map contains Ag, Au and C, all of the three latter seem to originate from the splashed particle. The sample is produced using two alloyed Ag25Au75 electrodes.*

SEM-EDS mapping of nanoparticles in a higher magnification is shown in figure 49. From the obtained element maps it is not clear that the signal originates from the nanoparticles. The Au map shows some indication of more signal from the area where the nanoparticles are.

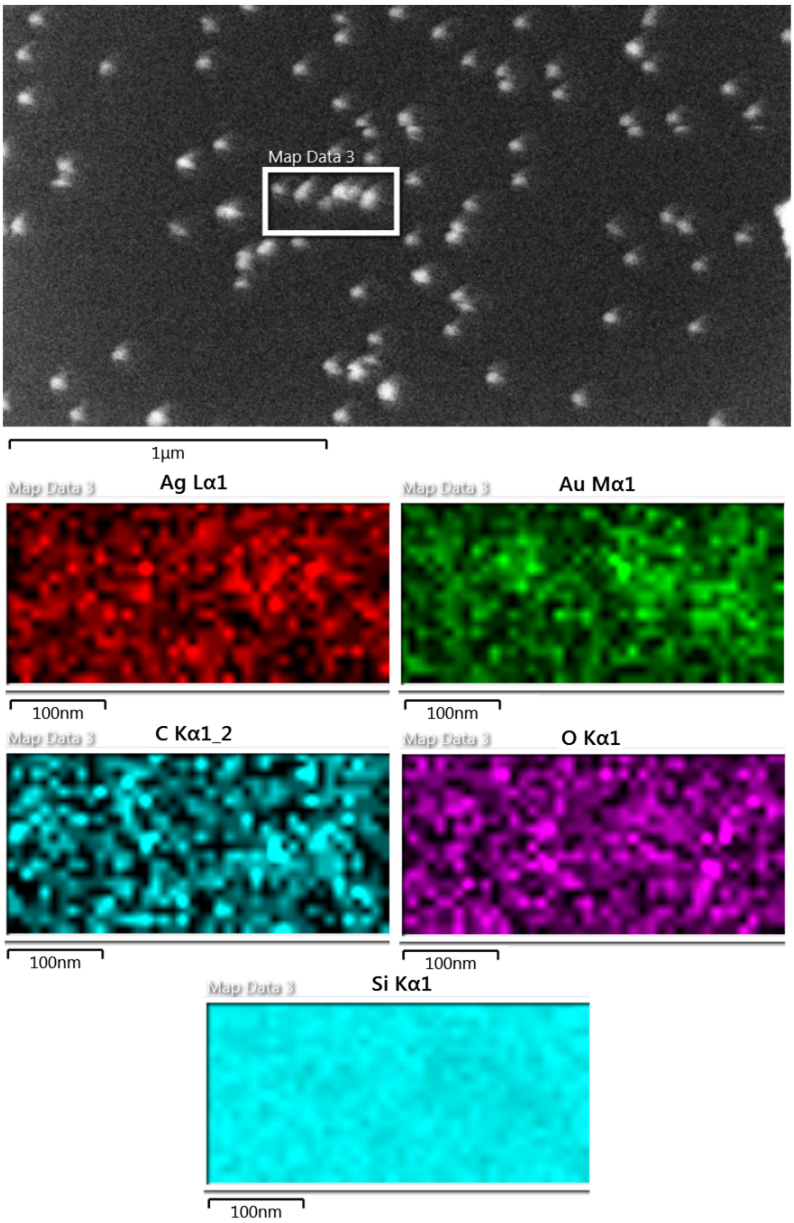

Figure 49: *SEM-EDS mapping of a few nanoparticles. Signal from Ag and Au can be detected, however, its origin can not be determined to be the nanoparticles. Other detected elements are C, O and Si. The sample is produced using two alloyed Ag25Au75 electrodes.*

SEM-EDS point spectra were acquired from each alloyed electrode. One example of a point spectrum acquired on an Ag25Au75 electrode is shown in figure 50 below. Characteristic peaks from both Ag and Au can be identified from the spectra. The composition obtained from the measurements of the electrodes are summarized in table 3. The obtained atomic percent Ag and Au of the alloyed electrodes seem to fit quite well with the electrode composition specified by Goodfellow. Deviation from the specified values of the electrode composition is assumed to be due to measurement errors. It should be noted that only one point spectra from each electrode was acquired, and for more reliable results, more spectras acquired in different locations on the electrode should be obtained, alternatively, some other method, for example ICP-MS, can be used.

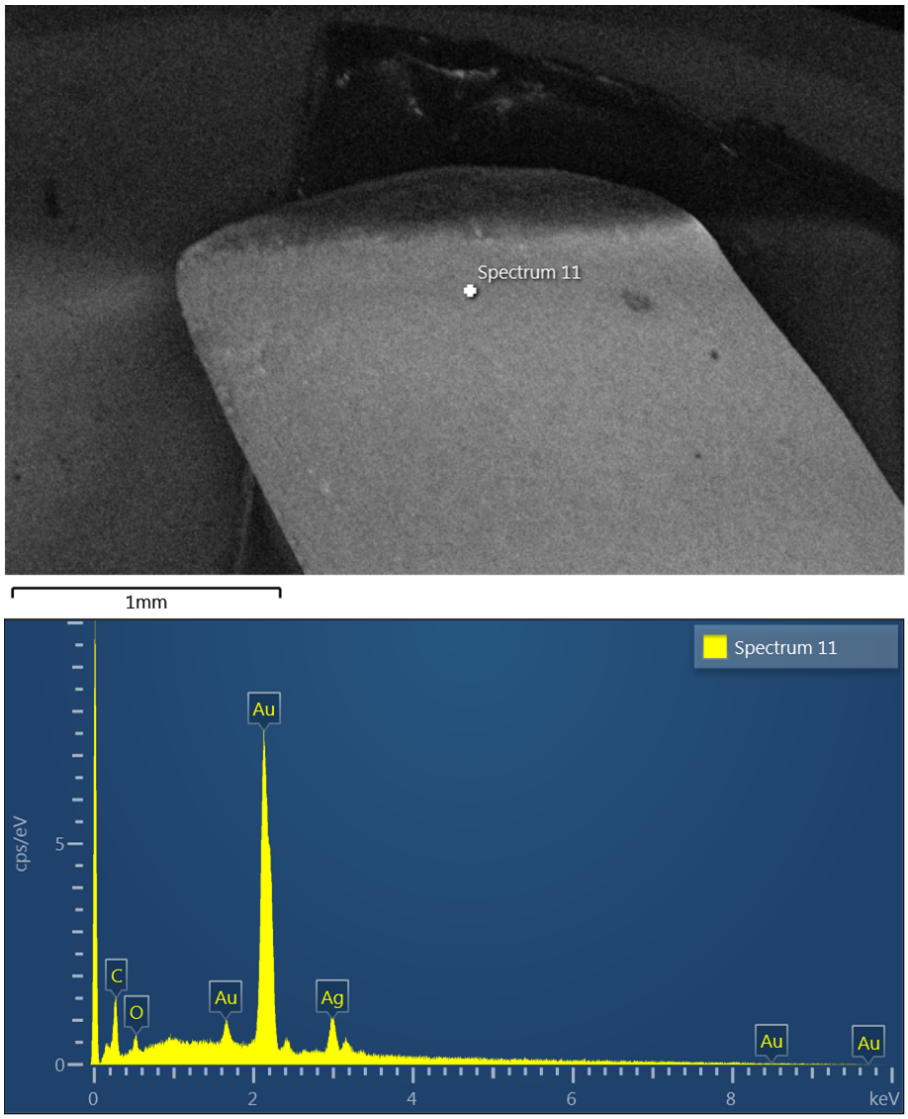

Figure 50: *SEM-EDS point spectra from an alloyed Ag25Au75 electrode. Ag and Au peaks are clearly visible.*

Table 3: *Composition of alloyed electrodes measured with SEM-EDS.*

Alloyed electrode	Ag25Au75	Ag50Au50	Ag75Au25
Ag content (at %)	26,8	51,4	76,0

XRD

Figure 51 shows the detected intensity from the XRD measurements of 30 nm Ag-Au nanoparticles generated using Ag25Au75 alloyed electrodes. Two lighter rings from the (111) and (200) lattice planes can be distinguished from the darker background, and one bright intensity spot is visible.

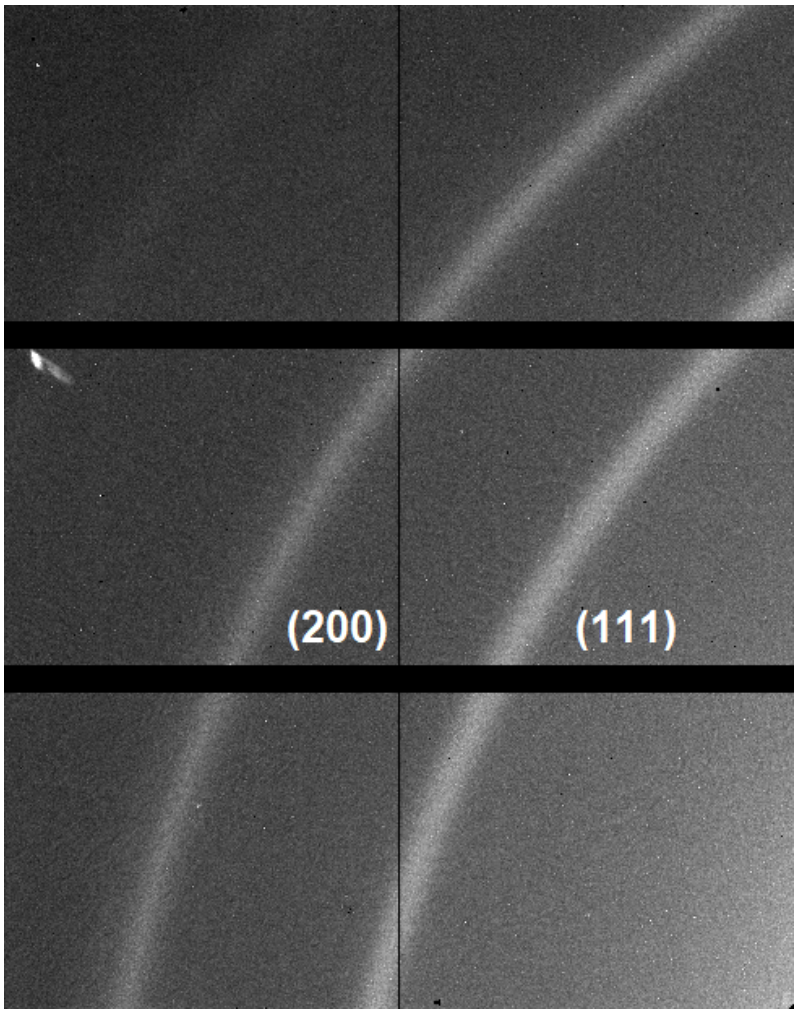

Figure 51: *XRD image showing two intensity rings from the (111) and (200) lattice planes and one diffraction spot in the left middle section. The tiny intensity grains are noise typically caused by dust particles in the air.*

Figure 52 shows the integrated intensity from figure 51 as a function of the diffracted angle. Reference data from powder XRD of pure Au and Ag are also plotted in the figure, and the peaks fit well to the peaks from the alloyed Ag-Au nanoparticles. The peaks correspond to the (111) and (200) lattice planes. The good fit with the reference data confirms that the nanoparticles contain either Ag or Au, or both. Since the Ag and Au peaks are practically superimposed on each other and not separated, it can not be determined if the nanoparticles consist of an alloyed Ag and Au phase using this technique. The smaller peak at about 23 degrees does not fit to reference data from Si (the substrate material) and is instead thought to originate from some material in the sample holder, but further investigations are needed.

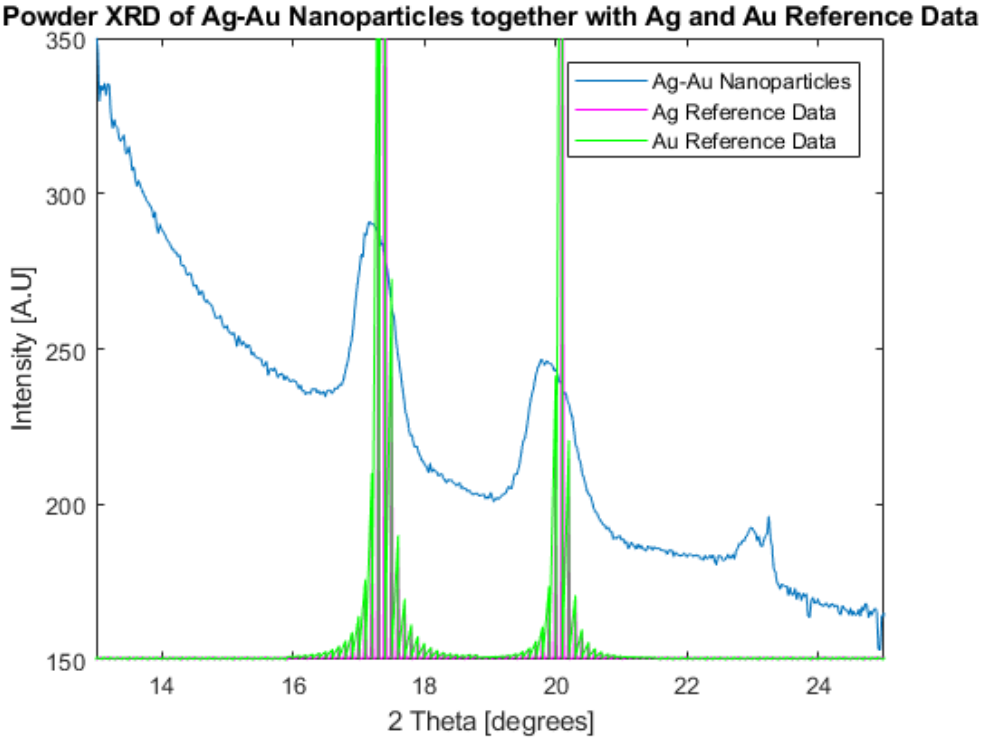

Figure 52: *Plot of the integrated intensity as a function of the angle 2 theta. The (111) and (200) peaks of the reference Ag and Au powder diffraction pattern coincides with the corresponding peaks of the nanoparticle measurement.*

5 Discussion

In this section, the most relevant results from this project will be discussed, e.g., the individual bimetallic particle compositions in relation to the composition of the electrodes used for particle production. The focus will be on particles produced by alloyed electrodes, though particles produced with two different electrodes also will be mentioned. The results will be compared to those previously reported, and discussed with focus on single particle versus ensemble composition measurements of spark ablated particles. The chapter ends with a discussion around the statistical analysis of the results acquired from the single particle measurements.

5.1 Quantitative Analysis of Nanoparticles

Little to no quantitative information about the nanoparticles could be obtained using the ensemble measurements obtained in the project, i.e., SEM-EDS and XRD. The quantification difficulties are thought to arise partly due to a too low deposited particle concentration (too low Ag and Au EDS-signal) for the SEM-EDS analysis, and partly due to the similar crystal structure and lattice parameters for Ag and Au, which are indistinguishable from each other and therefore not possible to use for quantification with XRD [47]. In the literature, XRD measurements of Ag-Au alloys have instead mainly been used to confirm crystallinity, or for obtaining size measurements [47] [48]. A higher coverage, similar to the coverage used for XRD, could be used in the future for obtaining ensemble measurements with SEM-EDS. Examples of other ensemble methods that could be used for quantification of the particles are X-ray photon spectroscopy (XPS) and ICP-MS. Both methods have been used in the literature to quantify the average composition of Ag-Au bimetallic nanoparticles [49][29]. Since the ensemble measurements performed in this project did not show how the particle composition is related to electrode composition, an investigation of what has been reported earlier in the literature for alloyed (and sintered) electrodes has been conducted.

A report that did acquire ensemble results from SEM-EDS of nanoparticles produced with Ni30Mo70 alloy electrodes [24] shows an average difference between the electrode composition and the nanoparticle composition of less than 3,3 atomic percent. It should also be mentioned that the standard deviation reported for these measurements are ± 2,00 atomic percent, and that they are based on 5 measurements. No quantitative single particle measurement of the particles was conducted. Another report [15] presenting ensemble measurements of agglomerated nanoparticles produced with Cr-Co alloyed electrodes (with a Cr/Co weight ratio of 0,37-0,51) showed an average weight ratio of 0,37 with an inductively coupled plasma (ICP) method, and a weight ratio of 0,58 with an XRD method. The large difference of the average compositions acquired with the two methods are thought to arise from extensive oxidation of the particles before the XRD measurement. No quantitative single particle measurements were conducted for the Cr-Co system. As an example of ensemble measurements performed on particles produced using mixed (sintered) electrodes, though not investigated in this project, a report [5] investigating nanoparticles of Cu and Ag produced from two sintered Cu-Ag electrodes is used. The Cu/Ag weight ratio in the nanoparticles measured by an ICP method was 0,388 and the Cu/Ag weight ratio in the electrodes was 0,380, a difference in composition of 2,1 percent between the nanoparticles and the electrodes. Evidently, the material system and the electrode composition are important for the resulting average nanoparticle composition, typically showing a difference in composition of

a few percent. Judging from the literature, the spark ablation community is good at presenting quantitative ensemble measurements of nanoparticles but might benefit from combining it with single particle measurements that can be compared to and help strengthen the acquired average results.

Single particle analysis using STEM-EDS and TEM-EDS in this project resulted in high signals from Ag and Au, allowing for reliable quantification of the nanoparticles. All quantified particles contained both Ag and Au, a fact that could only have been determined using single particle quantification methods, where TEM-EDS and STEM-EDS are great examples. As shown in table 2 the calculated average Ag content of the measured nanoparticles agree quite well (the highest deviation being 3,7 percent) with the corresponding alloyed electrode composition, true for both the TEM-EDS data from 2017 and 2021. The composition of the nanoparticles can therefore, from TEM-EDS quantification of single particles, be confirmed to agree with the corresponding alloyed electrode composition, for this particular material system. The fact that the measured compositions are not exactly the same as the electrode composition is attributed to the number of measurements, but also to measurement errors such as uncertainties in determining k-factors and in absorption correction during the EDS analysis. As a comparison, nanoparticles in the shape of agglomerates produced using alloyed electrodes of Cu40Ni60 and Cu70Ni30 are reported in [12] to have an average composition determined by STEM-EDS that differed with about 0,5 and 5 atomic percent respectively from the electrode composition. The larger deviation from the Cu70Ni30 sample was assumed to mainly be caused by measurement errors using EDS. However, there is no information available about how (what software, dead-time, or time constant used) the single particles were quantified using STEM-EDS, or how many particles that were characterized, making the results less trustworthy.

A report [2] where Pt-Pd agglomerate and compacted nanoparticles were generated using alloyed Pt50Pd50 showed, from TEM-EDS measurements of an unknown number of particles, a maximum deviation from the electrode composition of ± 0,75 at% and ± 1 at%. The authors attribute the deviation from the electrode composition to measurement errors in the EDS analysis. The results are similar to the ones obtained in this project, however, due to uncertainties regarding the number of particles analysed, the results become less trustworthy. Another example is a report [50] using alloyed Fe82,5Cr17,5 and Fe85Mn15 electrodes to produce nanoparticles with and without hydrogen in the carrier gas. The use of hydrogen in the carrier gas was to evaluate its influence on the oxidation and phase separation of the particles. Nanoparticles generated by the Fe-Cr electrodes show a mean Fe content obtained by STEM-EDS of about 40 individual particles (the number was acquired by asking the author, but was not available in the report) of 80 atomic percent (without hydrogen), and 84 atomic percent (with hydrogen). The difference between the electrode composition and the average nanoparticle composition was 2,5 and 1,5 atomic percent, respectively. STEM-EDS measurements of 21 (with hydrogen) and 25 (without hydrogen) nanoparticles generated with the Fe-Mn electrodes showed an average Fe content of 85 (without hydrogen) and 86 atomic percent (with hydrogen) indicating a difference in Fe content between the average nanoparticle and the electrode composition of 0 (without hydrogen) and 1 atomic percent (with hydrogen). The results are quite similar to the results obtained in this project with respect to the obtained difference between alloyed electrode composition and nanoparticle average

composition.

For the particles generated with one Ag and one Au electrode, the average Au composition from the TEM-EDS single particle measurements was about 77 atomic percent when Au was the anode, and about 79 atomic percent when Au was the cathode. The high Au content compared to Ag was expected due to the different ablatability ratios of the elements, and is in line with results from [29] in which one electrode of Ag and one of Au were used to produce nanoparticles by spark ablation. In the report, the average Au composition in the particles acquired by ICP-MS was 77 at% when Au was the anode, and 81 at% when Au was the cathode. The main goal of that report was to present the possibility to tune the composition of nanoparticles over a wide range (55-90 m/m% Au (where m/m% is thought to mean, but not clarified by the report, the mass Au in the particles divided by the total mass Au and Ag of the particles)) with the possibility to extend the range from 0 to 100 m/m% by controlling the spark, production parameters and by using alloyed electrodes. However, no quantitative single particle measurements were reported, and so the influence on the individual particle composition and the compositional variance among the nanoparticles are neglected. In [4] partly based on data from [15], one Pd electrode as anode and one Au electrode as cathode were used to produce nanoparticles whose single particle composition was determined by STEM-EDS measurements of 6 particles. The mean Pd/Au weight ratio from the STEM-EDS measurements was 0,26 with a standard deviation of 0,17. Such a high standard deviation can partly be explained by the low number of measurements (6 particles) and by the high ablatability ratio of Pd with Au (1,49 g/g Au). The average composition acquired from ICP-MS measurements in units of average mass Pd in the particles was 0,26. Though the average seems to be exactly the same for the single particle and the ensemble measurement methods, the values are given in different units, making it difficult as a reader to draw any conclusions about the difference of the measurements. Results presented in different units, not showing the number of particles measured or the obtained standard deviation or variance of the measurements, are commonly found in the literature of nanoparticles produced using the spark ablation method. Hence, there seems to exist a need for development of general strategies for obtaining and presenting reliable quantitative analysis- especially for individual particle analysis of nanoparticles produced using two different electrodes which are thought to exhibit a larger compositional variance than nanoparticles produced using alloyed electrodes.

5.2 Statistical Analysis of the Quantitative Results

From figure 42, 43 and 44 showing the composition distribution of the particles, the widths of the histograms are narrow and the sample standard deviations are low; less than about 1,6 atomic percent using alloyed electrodes (except for sample Ag25Au75 from 2017 where only 9 particles were measured), and less than about 3,3 atomic percent using two different electrodes. From literature it is known that the typical composition distribution differs between material systems, however, the low standard deviation obtained is surprising, compared to other reported standard deviations. One example is the report [50] mentioned in an earlier paragraph using alloyed Fe82,5Cr17,5 and Fe85Mn15 electrodes to produce nanoparticles with and without using hydrogen in the carrier gas. Nanoparticles generated by the Fe-Cr electrodes show a mean Fe content, obtained by STEM-EDS of about 40 individual particles, of 80 atomic percent (without hydrogen) and 84 atomic percent (with hydrogen). Both values show standard deviations of 2 atomic percent

and the difference between the electrode composition and the average nanoparticle composition was 2,5 and 1,5 atomic percent, respectively. STEM-EDS measurements of 21 (with hydrogen) and 25 (without hydrogen) nanoparticles generated with the Fe-Mn electrodes showed an average Fe content of 85 (without hydrogen) and 86 atomic percent (with hydrogen) with standard deviations of 3 atomic percent for both measurements [50]. The standard deviation of a few atomic percent of the average nanoparticle compositions are similar to the results from this project, especially convincing since both results are based on rigorous single particle analysis. Another report [16], with particles produced using one Cu and one Ag electrode, shows, from TEM-EDS measurements of 30 individual particles, a standard deviation of between 5 and 7 atomic percent depending on the compaction temperature of the particles. Since two different electrodes are used, the higher standard deviation compared to when particles are produced using alloyed electrodes was expected. The composition range of the nanoparticles is referred to as "narrow" by the authors. It is evident that the material system, the configuration and the composition of the electrodes influence the composition and the composition distribution of the produced nanoparticles. From the discussion, both similar and higher standard deviations of the composition of nanoparticles are reported in the literature compared to the results acquired in the project. It seems, however, that the deviations obtained in this project are low compared to reports of other material systems.

The reason for the low standard deviation obtained from the Ag-Au bimetallic nanoparticles is thought to partly depend on the number of particles measured. The higher the number of measurements of a sample distribution, the lower the estimated sample standard deviation becomes. However, the highest number of measurements (30 particles) were acquired of particles produced by one Ag and one Au electrode, showing a larger standard deviation than those obtained from fewer measurements (9-19 particles) of particles produced with alloyed electrodes. Evidently, the number of measurements is not the only contributing factor to the obtained standard deviations of the sample distributions, and it is concluded that particles produced with two different electrodes exhibit a higher variance than particles produced with alloyed electrodes. According to the mixing model for two different electrodes [4] described in section 2.1, the standard deviation can be influenced by the initial particle diameter, the final particle diameter and the mean particle composition. From the measurements in this project, the initial size of the particles in the vicinity of the spark can not be known. However, the initial particle size in the mixing model is thought to increase by using a large electrode gap, and decrease by having turbulent mixing near the spark, a low energy per spark and a high carrier gas flow. The production parameters used in this project have been held constant for all samples, and compared to parameters used in literature, the values are quite standard. For future experiments, it would be interesting to investigate the influence of the initial particle size on the sample standard deviation.

The final particle size is chosen (by using a DMA) to be 20 nm in diameter for all samples. The size is quite large for some applications (such as for catalysis) but is useful for EDS analysis since large particles typically provide more signal compared to smaller particles. According to the mixing model, large final particles can be a contributing factor for the low standard deviation obtained for the particles produced with two different electrodes. It would be interesting to investigate the influence of final particle size on the compositional sample standard deviation.

Another possible reason for the narrow distribution from the Ag-Au material system when using two different electrodes, according to the mixing model, is the mean particle composition. A mean composition dominated by one species is thought to decrease the sample standard deviation. For the Ag and Au system, it is known that Ag has a lower ablatability than Au and therefore it is more difficult to ablate material from the Ag electrode compared to from the Au electrode. The lower ablatability of Ag is confirmed by the compositional mean results of the particles produced with one Ag and one Au electrode, in both configurations of the electrodes. The fact that the mean composition is about the same when using the Ag as the anode and as the cathode despite theory stating that the negative electrode is ablated more strongly, further confirms the low ablatability of Ag compared to Au. Though there are several reports [4][14][29] trying to influence the mean composition by varying the nature of the spark, this has not been attempted in this project. It would be interesting to investigate the influence on the mean particle composition on the sample standard deviation by controlling the nature of the spark.

In the literature of spark ablated particles, it is not as common to report the variance of the particle composition as it is to report the sample standard deviation. The variance can, however, be used in an easy way to obtain the mean error of the variance estimation. Similar methods exist for estimating the mean error of the standard deviation, however, they are more difficult to use since they involve taking the square root of the variance which introduces a sample bias and has to be corrected for. By using the mean error of the variance, an indication of how good the sample variance estimates the real variance is obtained. From figure 45 it is clear that the sample variance is a good estimate for the samples produced using alloyed electrodes (apart from sample Ag25Au75 from 2017), and that it is less confident in estimating the population variance for the samples produced by alloyed electrodes. The mean error of the variance is sensitive to the sample size which partly is why sample Ag25Au75 from 2017 with a sample size of 9, has a high mean error of the variance. In fact, the factor which is multiplied with the variance to obtain the mean error of the variance, is almost twice as large for a sample of size 9 compared to one of size 30. This indicates the importance of performing multiple measurements of a sample when data with high confidence is preferred. The mean error of the variance also depends on the sample variance, which is higher for particles produced with two different electrodes compared to those from alloyed electrodes. Therefore, the samples produced with one Ag and one Au electrode have a higher value of the mean error even though a reasonably high number of measurements are acquired of those samples.

The 95% confidence intervals of the samples' means in figure 46 indicate similar results as the mean error of the variance. Apart from one sample (Ag25Au75 from 2017), the confidence intervals of the sample mean show narrow intervals of ± 1 atomic percent when using both alloyed and two different electrodes, though the latter intervals are somewhat larger. The confidence interval depends on the number of measurements and the sample standard deviation, which is why samples with few measurements or large standard deviations have a larger interval. The results indicate that the estimations of the populations' mean are good and that most samples have a mean that with 95% certainty lies within an interval of ± 1 atomic percent around the estimated mean. Confidence intervals of any sort have, to my knowledge, not been used in any previous report about spark ablated particles, and the obtained results can therefore not be compared to results in the literature. Future literature in the field of spark ablation might benefit from the inclusion

of confidence intervals as an alternative way to evaluate how good an estimation of a population mean is. Compared to standard deviations, confidence intervals of varying degrees of confidence can be chosen, depending on what certainty that is preferred for a measurement.

6 Conclusions & Outlook

The composition of Ag-Au bimetallic nanoparticles produced by spark ablation using both alloyed and two different electrodes have been investigated, and the particles have been analyzed using both ensemble and single particle characterization methods. We have, from rigorous single particle measurements, confirmed that particles produced using alloyed electrodes obtain the same composition as the electrodes, previously only indicated by the literature due to inadequate analysis. The use of single particle compositional analysis and not only ensemble measurements of the bimetallic particles was vital for confirming the presence of both Ag and Au in all measured particles, both from 2017 and 2021.

Particles produced using alloyed electrodes show the same average composition as the composition of the electrodes, with a maximum difference of 3,7 atomic percent. The mean composition standard deviation was lower than about 1,6 atomic percent (except for one sample where only 9 particles were measured and had a standard deviation of 4,2 atomic percent). Similar results from 2017 and from 2021 indicate a stable system with high reproducibility. For particles produced with one Ag and one Au electrode, the mean particle composition was about 20 atomic percent, with a standard deviation of 3,3 atomic percent or lower. The sample variance was lower for samples produced with alloyed electrodes (except for one sample from 2017) compared to samples produced with two different electrodes. The results are in line with the theory stating that alloyed electrodes produce nanoparticles with the same composition as the electrodes, and that particles produced by two different electrodes have a larger compositional distribution. However, even though the compositional variance is larger for particles produced with two different electrodes, the acquired sample standard deviation is low compared to results reported in the literature.

Statistical analysis of the composition of the particles have been conducted and has been compared to results in the literature. From reviewing the literature about spark ablated particles and their individual composition, if reported, it is clear that statistical analysis of the characterized particles rarely is performed, based on a low number of measurements, or presented in non-standard units. There seems to exist a need for developing general strategies for obtaining and presenting reliable quantitative analysis of individual particles in order to, in an easier way, interpret and compare results with each other. More precise and reliable results of the particles' individual composition might assist the development of nanoparticles with high performance that are attractive for industrial applications.

The obtained results are true for this material system, and it would therefore be interesting to also investigate other systems. The analysis could in the future also be extended to sintered electrodes which do not require for the elements to alloy in the bulk, allowing for a more flexible choice of materials. In this project, no reliable quantitative results from the ensemble measurements were obtained. For SEM-EDS a higher particle concentration might enable better analysis, while XRD just is not capable of quantifying Ag and Au due to their structural similarities. Further investigations of ensemble methods in combination with single particle quantification methods are needed. It would be interesting to see if ensemble methods (e.g., SEM-EDS, XPS, XRD and ICP-MS) produce the same sample mean as single particle methods (e.g., TEM-EDS and STEM) do.

One of the greatest advantages with the spark ablation method is the possibility to produce nanoparticles consisting of materials that do not mix in the bulk by using two different electrodes. In this project, tuning of the Ag-Au composition, when using one Au and one Ag electrode, was not attempted, but has been accomplished successfully in a recently published report [29] by controlling the oscillation of the spark. It would be very interesting to investigate the tuning capabilities of that and other material systems, and see how the compositional distribution changes as a result. More knowledge about the tuning capabilities of the composition of spark ablated nanoparticles will most likely help advance the position of spark ablation as a production method of bimetallic nanoparticles.

References

[1] Lesley E. Smart Elaine A. Moore. *Solid State Chemistry: An Introduction*. 4. CRC Press, Taylor and Francis Group, 2012. ISBN: 9781439847909.

[2] *Spark ablation : building blocks for nanotechnology*. Jenny Stanford Publishing, 2019. ISBN: 9789814800822.

[3] Jicheng Feng et al. "Magnetic Phase Transition in Spark-Produced Ternary LaFeSi Nanoalloys". In: *ACS Applied Materials & Interfaces* 10.7 (2018). PMID: 29372638, pp. 6073–6078. DOI: 10.1021/acsami.7b15441.

[4] J. Feng et al. "Internally mixed nanoparticles from oscillatory spark ablation between electrodes of different materials." In: *Aerosol Science and Technology* 52.5 (2018), pp. 505–514. ISSN: 15217388.

[5] Tabrizi N. et al. "Generation of mixed metallic nanoparticles from immiscible metals by spark discharge." In: *Journal of Nanoparticle Research* 12.1 (2010), pp. 247–259. ISSN: 13880764.

[6] Farid Bensebaa. "Chapter 1 - Nanoparticle Fundamentals". In: *Nanoparticle Technologies*. Ed. by Farid Bensebaa. Vol. 19. Interface Science and Technology. Elsevier, 2013, pp. 1–84. DOI: https://doi.org/10.1016/B978-0-12-369550-5.00001-X.

[7] N.S. Tabrizi and A. Schmidt-Ott. "The effect of operating conditions on the spark generated Au-Pd nanoparticles." In: *International Journal of Modern Physics: Conference Series*. Vol. 5. 1. Delft University of Technology, Faculty of Applied Sciences, Julianalaan 136, Delft, 2628 BL, Netherlands, 2860, 2012, pp. 291–298.

[8] Robert Hallberg. *Aerosol metal nanoparticles and their role in particle-assisted growth of III-V nanowires*. Division of Solid State Physics, Department of Physics, Faculty of Engineering, Lund University, 2018. ISBN: 9789177538431.

[9] F Jones. "Electrode Erosion by Spark Discharges". In: *British Journal of Applied Physics* 1 (Dec. 2002), p. 60. DOI: 10.1088/0508-3443/1/3/302.

[10] S. Schwyn, E. Garwin, and A. Schmidt-Ott. "Aerosol generation by spark discharge." In: *Journal of Aerosol Science* 19.5 (1988), pp. 639–642. ISSN: 00218502.

[11] Jicheng Feng et al. "General Approach to the Evolution of Singlet Nanoparticles from a Rapidly Quenched Point Source". In: *The Journal of Physical Chemistry C* 120.1 (2016), pp. 621–630. DOI: 10.1021/acs.jpcc.5b06503.

[12] A. Muntean et al. "Generation of copper, nickel, and CuNi alloy nanoparticles by spark discharge." In: *Journal of Nanoparticle Research* 18.8 (2016). ISSN: 1572896X.

[13] J.H. Byeon, J.H. Park, and J. Hwang. "Spark generation of monometallic and bimetallic aerosol nanoparticles." In: *Journal of Aerosol Science* 39.10 (2008), pp. 888–896. ISSN: 00218502.

[14] Shubhra Kala, Ralf Theissmann, and Frank Kruis. "Generation of AuGe nanocomposites by co-sparking technique and their photoluminescence properties." In: *Journal of Nanoparticle Research* 15.9 (2013), pp. 1–12. ISSN: 13880764.

[15] N.S. Tabrizi et al. "Synthesis of mixed metallic nanoparticles by spark discharge." In: *Journal of Nanoparticle Research* 11.5 (2009), pp. 1209–1218. ISSN: 13880764.

[16] Markus Snellman et al. "Continuous gas-phase synthesis of core–shell nanoparticles via surface segregation." In: *Nanoscale Advances* (2021). ISSN: 2516-0230.

[17] D.B. Williams and C.B. Carter. *Transmission Electron Microscopy: A Textbook for Materials Science*. Transmission Electron Microscopy: A Textbook for Materials Science v. 1. Springer, 1996. ISBN: 9780306453243.

[18] Chandan Srivastava et al. "Formation mechanism and composition distribution of FePt nanoparticles." In: *Journal of Applied Physics* 102.10 (2007), p. 104310. ISSN: 00218979.

[19] C Srivastava et al. "Investigation of Compositional Distribution During the Chemical Synthesis of FePt Nanoparticles". In: *Microscopy and Microanalysis* 13.S02 (2007), pp. 68–69. DOI: 10.1017/S1431927607077926.

[20] Stefano Cattaneo et al. "Synthesis of highly uniform and composition-controlled gold–palladium supported nanoparticles in continuous flow". In: *Nanoscale* 11 (17 2019), pp. 8247–8259. DOI: 10.1039/C8NR09917K.

[21] C.-Y. Wen et al. "Formation of Compositionally Abrupt Axial Heterojunctions in Silicon-Germanium Nanowires." In: *Science* 326.5957 (2009), pp. 1247–1250. ISSN: 00368075.

[22] S. Jahn et al. "Precise AuxPt1-x Alloy Nanoparticle Array of Tunable Composition for Catalytic Applications." In: *Scientific Reports* 6 (2016). ISSN: 20452322.

[23] Attila Kohut et al. "Facile and versatile substrate fabrication for surface enhanced Raman spectroscopy using spark discharge generation of Au/Ag nanoparticles." In: *Applied Surface Science* 531 (2020). ISSN: 0169-4332.

[24] Hatoon Makhool. "Generation of Model NiMo Hydrotreating Nano-catalysts via the Spark Discharge Technique". In: (2020). ISSN: 0280-5316.

[25] S. Blomberg et al. "Generation and oxidation of aerosol deposited PdAg nanoparticles". In: *Surface Science* 616 (2013), pp. 186–191. ISSN: 0039-6028. DOI: https://doi.org/10.1016/j.susc.2013.06.005.

[26] Blomberg Sara et al. "Bimetallic Nanoparticles as a Model System for an Industrial NiMo Catalyst." In: *Materials* 12.22 (2019), p. 3727. ISSN: 1996-1944.

[27] B. O. Meuller et al. "Review of spark discharge generators for production of nanoparticle aerosols". In: *Aerosol Science and Technology* 46.11 (2012). Cited By :71, pp. 1256–1270.

[28] N. S. Tabrizi et al. "Generation of nanoparticles by spark discharge." In: *JOURNAL OF NANOPARTICLE RESEARCH* 11.2 (2009), pp. 315–332. ISSN: 13880764.

[29] Attila Kohut et al. "Full range tuning of the composition of Au/Ag binary nanoparticles by spark discharge generation." In: *Scientific Reports* 11.1 (2021), pp. 1–10. ISSN: 20452322.

[30] Assoc.Prof.Dr. Panich Intra and Nakorn Tippayawong. "An overview of differential mobility analyzers for size classification of nanometer-sized aerosol particles". In: *Songklanakarin Journal of Science and Technology* 30 (Mar. 2008).

[31] M. Karlsson et al. "Compaction of agglomerates of aerosol nanoparticles: A compilation of experimental data". In: *Journal of Nanoparticle Research* 7 (Feb. 2005), pp. 43–49. DOI: 10.1007/s11051-004-7218-3.

[32] C. Preger et al. "Predicting the deposition spot radius and the nanoparticle concentration distribution in an electrostatic precipitator." In: *Aerosol Science and Technology* 54.6 (2020), pp. 718–728. ISSN: 15217388.

[33] TSI Incorporated. *AEROSOL ELECTROMETER 3068B*. 2021. URL: https://tsi.com/products/particle-counters-and-detectors/aerosol-electrometer/aerosol-electrometer-3068b/ (visited on 05/26/2021).

[34] Claudionico. *Electron Interaction with Matter*. 2013. URL: https://commons.wikimedia.org/w/index.php?curid=44224781.

[35] Sdk16420. *Bright field TEM*. 2015. URL: https://commons.wikimedia.org/w/index.php?curid=41721529.

[36] David C. Joy et al. *Scanning Electron Microscopy and X-Ray Microanalysis*. Springer, 2018. ISBN: 9781493966745.

[37] Oxford Instruments. *AZtecLive - In Depth*. 2021. URL: nano.oxinst.com/campaigns/downloads/azteclive-in-depth-tru-q.

[38] Aboalbiss. *Bragg's Law*. 2009. URL: https://commons.wikimedia.org/w/index.php?curid=8452301.

[39] XanaG. *Si powder diffraction pattern indexed*. 2012. URL: https://commons.wikimedia.org/w/index.php?curid=18506978.

[40] Wheeler P. Davey. "Precision Measurements of the Lattice Constants of Twelve Common Metals". In: *Phys. Rev.* 25 (6 June 1925), pp. 753–761. DOI: 10.1103/PhysRev.25.753. URL: https://link.aps.org/doi/10.1103/PhysRev.25.753.

[41] Esteteiu. *XRD Cerium oxide*. 2020. URL: https://commons.wikimedia.org/w/index.php?curid=96221547.

[42] Metallos. *Ag-Au-phase-diagram-greek*. 2007. URL: https://commons.wikimedia.org/w/index.php?curid=11448110.

[43] Gurland John and Tripathi Ram C. "A Simple Approximation for Unbiased Estimation of the Standard Deviation." In: *The American Statistician* 25.4 (1971), pp. 30–32. ISSN: 00031305.

[44] Lennart Olbjer. *Experimentell och Industriell Statistik*. Matematikcentrum, 2000.

[45] Saulius Gražulis et al. "Crystallography Open Database (COD): an open-access collection of crystal structures and platform for world-wide collaboration". In: *Nucleic Acids Research* 40.D1 (2012), pp. D420–D427. DOI: 10.1093/nar/gkr900.

[46] A. Kohut et al. "Surface features and energy considerations related to the erosion processes of Cu and Ni electrodes in a spark discharge nanoparticle generator." In: *Journal of Aerosol Science* 119 (2018), pp. 51–61. ISSN: 0021-8502.

[47] Ai-Qin Wang et al. "A novel efficient Au–Ag alloy catalyst system: preparation, activity, and characterization". In: *Journal of Catalysis* 233.1 (2005), pp. 186–197. ISSN: 0021-9517. DOI: https://doi.org/10.1016/j.jcat.2005.04.028.

[48] G. Suyal, M. Mennig, and H. Schmidt. "Synthesis of nanocomposite thin films containing Ag-Au alloy colloids for wavelength tunability." In: *Journal of Materials Science* 38.8 (2003), pp. 1645–1651.

[49] Malathi Sampath et al. “One pot green synthesis of Ag, Au and Au-Ag alloy nanoparticles using isonicotinic acid hydrazide and starch”. In: *Carbohydrate polymers* 111C (Oct. 2014), pp. 734–743. DOI: 10.1016/j.carbpol.2014.04.105.

[50] Calle Preger et al. “Controlled Oxidation and Self-Passivation of Bimetallic Magnetic FeCr and FeMn Aerosol Nanoparticles.” In: *Journal of Physical Chemistry C* 123.26 (2019), pp. 16083–16090. ISSN: 1932-7447.